
GEOMETRY-AWARE BAYESIAN QUANTIFICATION VIA COMPOSITIONAL DATA ANALYSIS

Alejandro Moreo

Istituto di Scienza e Tecnologie dell'Informazione
Consiglio Nazionale delle Ricerche
Pisa, Italy
alejandro.moreo@isti.cnr.it

Pablo González, Juan José del Coz

Artificial Intelligence Center
University of Oviedo
Asturias, Spain
{gonzalezpablo,juanjo}@uniovi.es

July 7, 2026

ABSTRACT

Accurately estimating the unknown target label distribution is the critical first step for adapting to label shift. This task, widely known as quantification or class prevalence estimation, has recently seen significant advances through continuous KDE-based methods which model the density of multiclass classifier posteriors. Posterior vectors might be regarded as compositional data, since they lie on the probability simplex. However, existing KDE-based quantifiers typically rely on Euclidean Gaussian kernels, which ignore simplex geometry and incorrectly assign probability mass outside its boundaries. We introduce a geometry-aware KDE model for multiclass quantification based on log-ratio representations and Aitchison geometry, together with a shrinkage regularization that improves robustness near the simplex boundary. Combined with a maximum-likelihood interpretation of KDE-based quantification, we derive both point-estimation and Bayesian inference procedures for class prevalences. Experiments on 42 datasets across tabular, text, and image domains show that the proposed method is competitive with state-of-the-art quantifiers, often improving over standard KDE-based baselines, while also yielding strong results among Bayesian quantification methods.

1 Introduction

Machine learning models deployed in the wild frequently encounter label shift [41]. Adapting to this shift requires accurately estimating the unknown target label distribution. This problem, called quantification [16] or class prevalence estimation [31], is a critical standalone task in domains where aggregate population trends matter more than individual predictions. Furthermore, it serves as the essential foundation for label shift adaptation, as accurate prevalence estimates are strictly required to compute importance weights for classifier retraining [3].

Many prominent methods, such as Maximum Likelihood for Label Shift (MLLS) [38] and Black-Box Shift Estimation (BBSE) [31], operate directly on the posterior probabilities produced by a base classifier. In multiclass quantification, modeling the continuous distribution of these posteriors using density-based methods like KDEy [35] has emerged as a powerful alternative that naturally preserves the dependence structure across classes. Consequently, KDEy is increasingly adopted as a robust solution in a variety of application domains, such as fairness monitoring in IR [27], graph-related applications [8, 33], classifier accuracy prediction [44], and medical imaging for healthcare [20].

However, modeling classifier posteriors via continuous density estimation introduces a fundamental geometric mismatch. Posterior probability vectors lie on the probability simplex and therefore constitute compositional data. Existing KDE-based quantifiers rely on Gaussian kernels in Euclidean space, which ignore this relative structure and inevitably assign probability mass outside the simplex boundaries. This mismatch becomes particularly problematic near the boundary of the simplex, where posterior probabilities heavily concentrate in many real-world settings.

In this work, we revisit multiclass quantification from the perspective of compositional data analysis (CoDA) [1] to resolve this bottleneck. We introduce a geometry-aware kernel based on log-ratio transformations, enabling continuous density estimation in Aitchison geometry. While this representation is more consistent with the underlying simplex

structure, naive log-ratio modeling can be unstable near the boundary. To address this issue, we propose a shrinkage-based regularization that improves robustness. Building on this representation, we formulate quantification as a mixture density estimation problem that naturally admits both point estimation and Bayesian inference over class prevalences. Across 42 datasets spanning tabular, textual, and image domains, the proposed method achieves performance that is competitive with state-of-the-art approaches. It frequently improves over standard KDE-based quantifiers, while providing a principled geometric formulation of continuous density estimation on the simplex.

2 Related Work

The literature on label shift adaptation and quantification primarily focuses on the setting of label shift (aka prior probability shift) [41]. Existing approaches include classify-and-count variants (e.g., BBSE [31], also known in the quantification literature as Adjusted Classify and Count (ACC) [16] or the confusion matrix approach in [38]), distribution matching methods [21, 5, 11], and maximum likelihood approaches via expectation maximization (e.g., MLLS, often referred to as EMQ in quantification literature) [38, 4, 3]. Among these, KDE-based methods such as KDEy have recently emerged as strong performers in the multiclass setting [35].

Bootstrap-based approaches have been explored for deriving uncertainty estimates in quantification [24, 9, 42]. Analytical approaches to confidence interval estimation have also been developed for specific estimators [14, 10]. More recently, Bayesian quantification methods have been proposed for standard quantifiers [15]; examples include BayesianACC¹ for BBSE/ACC, MAPLS [46, 25] for MLLS/EMQ, and Precise Quantifier (PQ) [26] for HDy [21]. However, the multinomial model over binned probabilities used by PQ (an analogue of HDy’s histogram representation) inherits the limitations of univariate, discretized density models and is thus restricted to binary problems. Such limitations are overcome by continuous multivariate density models based on KDE [35]. Nevertheless, no prior work has developed a Bayesian formulation for KDE-based quantifiers; we fill this gap.

We also note that KDE models based on Gaussian kernels may be inappropriate for compositional data. Simplex-supported alternatives to Euclidean KDE do exist in the compositional-data literature, most notably Dirichlet-kernel and logistic-normal-kernel estimators [2]. Subsequent work has further developed the log-ratio route, in particular through Gaussian kernels defined in isometric log-ratio (ILR) coordinates together with modern bandwidth-selection methods, suggesting that this line is especially natural when the goal is to respect the geometry of compositional data [6, 32]. At the same time, Dirichlet kernels remain theoretically attractive because they are natively supported on the simplex and exhibit favorable boundary behavior [37]. In practice, applying standard compositional kernels directly to classifier outputs is difficult, as confident predictions cause (presumably well-calibrated) posteriors to concentrate heavily at the simplex boundaries. Furthermore, unlike standard Euclidean KDEs, these simplex-aware estimators lack drop-in implementations for ML pipelines. By introducing a shrinkage-regularized log-ratio representation, we bridge these gaps, providing a mathematically principled yet computationally practical solution.

3 Problem Setup

Let \mathcal{X} denote the input space and $\mathcal{Y} = \{1, \dots, K\}$ the set of class labels. We assume a standard prior probability shift setting [41], where training and test data are drawn from distributions P_s and P_t , respectively, such that $P_s(Y) \neq P_t(Y)$, and $P_s(X | Y) = P_t(X | Y)$.

We assume access to a probabilistic classifier $s : \mathcal{X} \rightarrow \Delta^{K-1}$, which maps each input $x \in \mathcal{X}$ to a posterior probability vector $p = s(x) = (p_1, \dots, p_K)$, where $p_k = \hat{P}_s(Y = k | x)$. Here, Δ^{K-1} denotes the probability simplex $\Delta^{K-1} = \{p \in \mathbb{R}^K : p_k \geq 0, \sum_{k=1}^K p_k = 1\}$.

Since $p = s(X)$ is a deterministic, measurable transformation of X , the class-conditional distributions of posterior probabilities are also invariant across domains, i.e., $P_s(p | Y) = P_t(p | Y)$; see Lemma 1 in [31]. This allows us to perform quantification directly in the space of posterior probabilities.

Let $\mathcal{U} = \{x_1, \dots, x_n\}$ denote an unlabeled sample drawn from P_t , and let $\mathcal{P} = \{p^{(1)}, \dots, p^{(n)}\}$, with $p^{(i)} = s(x_i)$, be the corresponding set of posterior probability vectors. The goal of quantification is to estimate the class prevalence vector $\pi = (\pi_1, \dots, \pi_K) \in \Delta^{K-1}$, where $\pi_k = P_t(Y = k)$.

Remark 1. Let f_1, \dots, f_K denote class-conditional densities, and consider the mixture model $m_\pi(p) = \sum_{k=1}^K \pi_k f_k(p)$, with $\pi \in \Delta^{K-1}$. Let $\mathcal{P} = \{p^{(1)}, \dots, p^{(n)}\}$ be the observed posterior probability vectors in the target sample. At the

¹Introduced as BayesianCC by Ziegler and Czyż [47]. We use the term BayesianACC to maintain consistent terminology and reflect its mathematical equivalence to ACC (BBSE) rather than to CC (which often denotes plain “Classify and Count”).

population level, quantification can be viewed as a distribution matching problem in which the target density q is approximated by the mixture m_π . When matching is formalized via the Kullback–Leibler divergence, one obtains

$$\arg \min_{\pi \in \Delta^{K-1}} D_{\text{KL}}(q \parallel m_\pi) = \arg \max_{\pi \in \Delta^{K-1}} \mathbb{E}_q[\log m_\pi(p)].$$

Replacing the expectation by its empirical counterpart yields the maximum likelihood estimator [18]

$$\hat{\pi} = \arg \max_{\pi \in \Delta^{K-1}} \sum_{i=1}^n \log m_\pi(p^{(i)}). \tag{1}$$

Following [35], we model the densities f_k using class-conditional kernel density estimators.

4 Geometric Mismatch in KDE-Based Quantification

The KDE-based formulation introduced above operates on classifier posterior probabilities $p \in \Delta^{K-1}$. This is already a substantial simplification with respect to working directly in the original input space \mathcal{X} , and has proven highly effective in multiclass quantification [35]. However, posterior probability vectors are not ordinary Euclidean data: they are *compositions*, i.e., non-negative vectors constrained to sum to one. As such, they live on the probability simplex and are more naturally studied within the framework of compositional data analysis (CoDA) [1].

The constraint by which posterior vectors $p = (p_1, \dots, p_K)$ lie in the simplex induces a non-Euclidean geometry: the components of p are not independent coordinates, and meaningful comparisons are inherently relative. In particular, compositions are more naturally compared through log-ratios than through Euclidean differences in the ambient space \mathbb{R}^K . Standard KDE-based quantifiers, including KDEy, estimate class-conditional densities of posterior vectors using Gaussian kernels in Euclidean space. This introduces a geometric mismatch for two related reasons. First, Gaussian kernels on the ambient space \mathbb{R}^K assign non-zero probability mass outside the simplex. Second, Euclidean distance does not respect the relative structure of compositions, and may therefore distort similarity relationships between posterior vectors. This mismatch is not merely aesthetic. Since the quantifier ultimately estimates prevalences by fitting a mixture model to the empirical distribution of posterior vectors, misspecifying the geometry of the data may lead to distorted density estimates and, consequently, biased or unstable prevalence predictions.

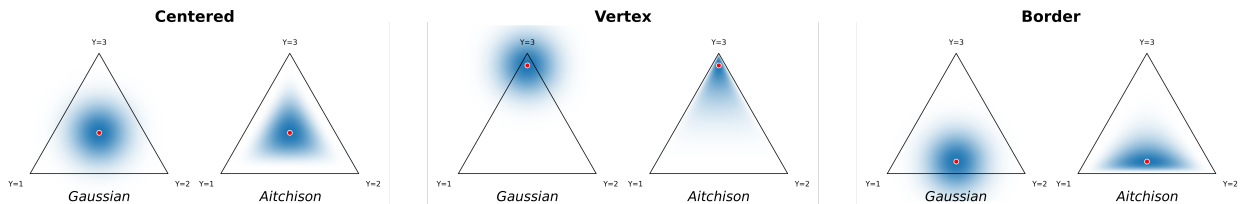


Figure 1: Comparison between a standard Gaussian kernel in Euclidean space and a geometry-aware kernel induced through a log-ratio representation. Near the boundary of the simplex, the Gaussian kernel assigns probability mass outside the support, whereas the geometry-aware alternative better respects the simplex structure.

The geometric mismatch is particularly severe near the boundary of the simplex. In many realistic classification problems, posterior vectors tend to concentrate near vertices or edges, corresponding to confident predictions or highly imbalanced uncertainty across classes. This is especially true for neural classifiers, which are known to be overconfident, in which case posterior calibration is required [22]. In such regions, Euclidean Gaussian kernels place a non-negligible fraction of their mass outside the simplex, precisely where the support constraint is most restrictive. At the same time, the natural tools from CoDA (namely, log-ratio transformations such as the centered log-ratio (CLR) and isometric log-ratio (ILR) maps) become increasingly sensitive near the boundary, where some coordinates approach zero. This creates a tension: while log-ratio geometry is more appropriate for simplex-valued data, a naive application of CLR/ILR may itself become unstable in the regime where geometric mismatch matters most. Figure 1 illustrates this effect.

These observations suggest that density-based quantification should be performed in a geometry-aware representation of the simplex, rather than in the ambient Euclidean space. In the next section, we develop such a representation using log-ratio coordinates. We further show that, although CLR/ILR provide the correct geometric framework, additional regularization is needed to obtain stable density estimates near the simplex boundary.

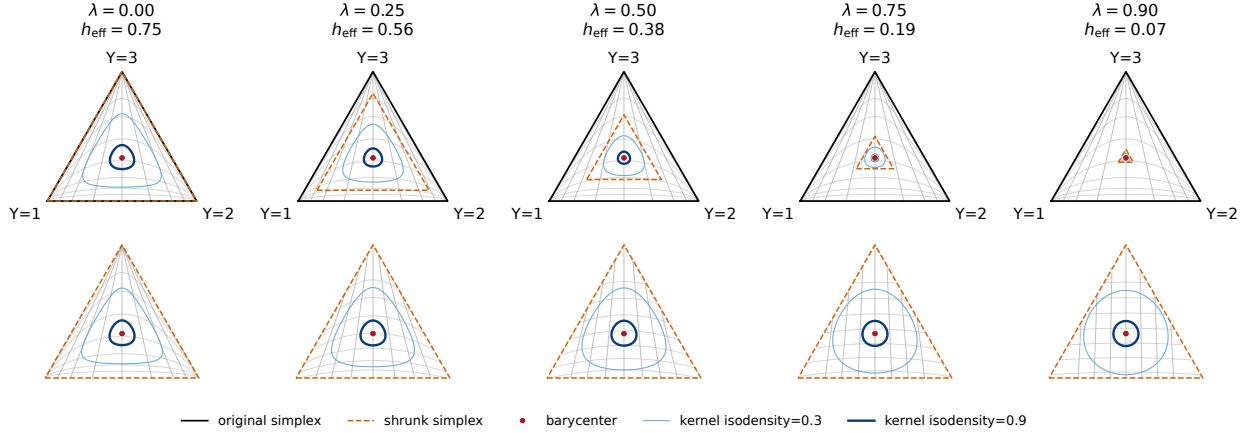


Figure 2: Effect of shrinkage on a geometry-aware kernel centered in the simplex for $h = 0.75$. As λ increases, the effective simplex contracts towards the barycenter. The first row show the shrinkage from the point of view of the original simplex, while the second row is a zoom in the effective shrunk region. By adjusting h_{eff} , the induced kernel becomes locally Euclidean for high values of λ .

5 Shrinkage-Regularized Geometry-Aware KDE

Let $p \in \Delta^{K-1, \circ}$ be a posterior probability vector. We consider log-ratio transformations $\phi : \Delta^{K-1, \circ} \rightarrow \mathbb{R}^{K-1}$ or to the zero-sum subspace of \mathbb{R}^K , in particular the isometric log-ratio (ILR) and the centered log-ratio (CLR) maps from CoDA, respectively. These transformations provide Euclidean coordinates consistent with Aitchison geometry, thereby enabling density estimation in a representation that respects the relative structure of compositions. In practice, both CLR and ILR lead to equivalent distance-based behavior, since ILR is an isometric reparameterization of CLR restricted to the zero-sum subspace. We therefore use CLR in our implementation for computational convenience, while the same construction applies to ILR. From this point onward, we let ϕ denote the CLR transformation, defined as

$$\phi(p) = \left(\log \frac{p_1}{g(p)}, \dots, \log \frac{p_K}{g(p)} \right), \quad g(p) = \left(\prod_{k=1}^K p_k \right)^{1/K},$$

where $g(p)$ denotes the geometric mean of the components of p .

Despite their geometric appeal, log-ratio coordinates are delicate near the boundary of the simplex. Whenever one or more components of p approach zero, the corresponding log-ratios become large in magnitude, which may induce unstable density estimates and highly distorted local geometries. This is particularly problematic in quantification, where posterior probabilities may legitimately attain zero or near-zero values. To mitigate this issue, we introduce a shrinkage transformation that moves each composition away from the boundary and towards the simplex barycenter $u = (\frac{1}{K}, \dots, \frac{1}{K})$:

$$T_\lambda(p) = (1 - \lambda)p + \lambda u, \quad \lambda \in [0, 1].$$

When $\lambda = 0$, the original composition is recovered. As λ increases, $T_\lambda(p)$ contracts the simplex towards its center, ensuring that all transformed compositions remain bounded away from zero.

Shrinkage has two complementary effects. First, it prevents numerical instability in the log-ratio map. Second, it regularizes the geometry of the transformed space near the simplex boundary, where the nonlinear effects of ϕ are most severe. Importantly, this does not simply recover the original Euclidean KDE. Rather, shrinkage moves the problem into a regime where the log-ratio representation becomes locally well behaved, while preserving the compositional structure of the data. The goal is not to discard simplex geometry, but to regularize its most unstable regime.

Because shrinkage contracts the effective simplex towards the barycenter, the bandwidth must be adjusted accordingly to preserve a comparable amount of smoothing across values of λ . Under the affine shrinkage map T_λ , distances in the simplex hyperplane are uniformly rescaled by the factor $1 - \lambda$. Therefore, if h denotes the bandwidth before shrinkage, the natural effective bandwidth becomes $h_{\text{eff}} = (1 - \lambda)h$. More generally, since the intrinsic dimension of the simplex is $K - 1$, the corresponding density height rescales by the Jacobian factor $(1 - \lambda)^{-(K-1)}$. A full derivation is provided in Appendix B.

Figure 2 illustrates the combined effect of shrinkage and bandwidth rescaling on an Aitchison-centered kernel. The regularizing effect of shrinkage can be formalized by studying the behavior of ϕ near the barycenter.

Proposition 1. Let $u = (\frac{1}{K}, \dots, \frac{1}{K})$, let ϕ denote the CLR map, and write $T_\lambda(p) = u + (1 - \lambda)(p - u)$. Then, for any fixed $p \in \Delta^{K-1, \circ}$,

$$\phi(T_\lambda(p)) = K(1 - \lambda)(p - u) + O((1 - \lambda)^2) \quad \text{as } \lambda \rightarrow 1.$$

This shows that shrinkage attenuates the nonlinear effects of the CLR transformation: the leading term is linear in $1 - \lambda$, while the nonlinear remainder is of second order. Hence, shrinkage regularizes the geometry precisely in the regime where log-ratio representations would otherwise be most unstable. A full proof is provided in Appendix A.

This local linearization also has an estimator-level implication. When combined with the bandwidth scaling $h_{\text{eff}} = (1 - \lambda)h$, the induced Gaussian kernel in transformed coordinates is locally well approximated by a Euclidean Gaussian kernel on the simplex hyperplane, up to a multiplicative constant and higher-order local terms. In this sense, shrinkage places the geometry-aware estimator in a locally Euclidean regime near the barycenter, without collapsing it into an ordinary Euclidean KDE. A heuristic derivation is provided in Appendix C.

5.1 Geometry-aware KDE

Given the transformed representation $z = \phi(T_\lambda(p))$, we estimate class-conditional densities in the transformed space by standard kernel density estimation. For each class $k \in \{1, \dots, K\}$, let $\mathcal{Z}_k = \{z_i : y_i = k\}$ denote the transformed training posteriors for class k . We then define

$$f_k^h(z) = \frac{1}{|\mathcal{Z}_k|} \sum_{z' \in \mathcal{Z}_k} \mathcal{K}_{h_{\text{eff}}}(z - z'), \quad (2)$$

where $\mathcal{K}_{h_{\text{eff}}}$ is a Gaussian kernel with effective bandwidth $h_{\text{eff}} = (1 - \lambda)h$ (refer to Appendix B for the mathematical derivation). This yields a shrinkage-regularized, geometry-aware instantiation of the class-conditional densities.

We now turn to showing that this model naturally supports both Bayesian posterior inference and point estimation over the prevalence vector π . Let $z = \phi(T_\lambda(p))$, where ϕ denotes the fixed CLR transformation and T_λ the fixed shrinkage map. For each class $k \in \{1, \dots, K\}$, let $f_k^h(z)$ denote the corresponding class-conditional density estimate in the transformed space (Equation 2). We redefine the prevalence-dependent mixture:

$$m_\pi(z) = \sum_{k=1}^K \pi_k f_k^h(z), \quad \pi \in \Delta^{K-1}.$$

Although density estimation is carried out in transformed coordinates, the observed posterior vectors $p^{(1)}, \dots, p^{(n)}$ live on the simplex. Therefore, the exact density induced on the simplex must account for the change of variables. For any $p \in \Delta^{K-1, \circ}$, the corresponding exact density is

$$q_\pi(p) = J_{\phi \circ T_\lambda}(p) m_\pi(\phi(T_\lambda(p))),$$

where $J_{\phi \circ T_\lambda}(p)$ denotes the Jacobian term induced by the transformation $\phi \circ T_\lambda$. Since the Jacobian does not depend on π , the exact likelihood for a test sample $\mathcal{P} = \{p^{(1)}, \dots, p^{(n)}\}$ satisfies

$$\mathcal{L}_{\text{exact}}(\pi; \mathcal{P}) = \prod_{i=1}^n J_{\phi \circ T_\lambda}(p^{(i)}) \left(\sum_{k=1}^K \pi_k f_k^h(z^{(i)}) \right) \propto \prod_{i=1}^n \left(\sum_{k=1}^K \pi_k f_k^h(z^{(i)}) \right),$$

where $z^{(i)} = \phi(T_\lambda(p^{(i)}))$. Thus, the Jacobian term does not need to be evaluated explicitly.

5.2 Bayesian posterior inference

The previous result immediately yields a Bayesian formulation of geometry-aware KDE quantification. Given a prior $p(\pi)$ on the prevalence vector, the posterior distribution is

$$p(\pi | \mathcal{P}) \propto p(\pi) \mathcal{L}_{\text{exact}}(\pi; \mathcal{P}) \propto p(\pi) \prod_{i=1}^n \left(\sum_{k=1}^K \pi_k f_k^h(z^{(i)}) \right). \quad (3)$$

Thus, although the exact simplex density formally includes a Jacobian term, posterior inference can be carried out directly in transformed coordinates using the unnormalized posterior above. This is the key observation that makes Bayesian inference practical for KDE-based quantification. Note that the same cancellation argument applies to point estimation, since multiplicative constants independent of π do not affect the argmax in Equation 1 under the change of variables.

To control posterior dispersion under misspecification, we consider a tempered posterior of the form

$$p_T(\pi | \mathcal{P}) \propto p(\pi) \left[\prod_{i=1}^n \left(\sum_{k=1}^K \pi_k f_k^h(z^{(i)}) \right) \right]^{1/T}, \quad T > 0.$$

The temperature parameter T leaves the density model unchanged and primarily controls posterior concentration. In practice, T is selected on a held-out calibration split; see Section 6.

6 Experiments

Datasets. We evaluate on 42 datasets spanning text, tabular, and image domains, with numbers of classes ranging from 2 to 100, used in previous related research. The text suite includes the standard LeQua benchmarks [12, 13] and 11 Twitter sentiment datasets [17]; the tabular suite contains 22 UCI ML datasets [28]; the image suite includes CIFAR10/CIFAR100 [29], MNIST [30], FashionMNIST [45], and SVHN [36]. Full dataset statistics are given in Appendix D.1.

Base classifiers and baselines. For text and tabular data, we use logistic regression (LR) on fixed features (neural embeddings provided by the LeQua creators², and TF-IDF weighted vectors for Twitter data available online³) since LR is the standard choice in the quantification literature as it natively provides well calibrated posterior probabilities [39]. For image data, we use ResNet18 (CIFAR/SVHN) or a lightweight CNN (MNIST/FashionMNIST), with calibrated posteriors obtained via BCTS following [3]. We consider a representative set of baselines covering classical point estimators, density-based methods, and available Bayesian quantifiers. Specifically, we compare against a naive ‘‘classify and count’’ (CC) [16], its probabilistic counterpart (PCC) [16], BBSE/ACC [31], MLLS/EMQ [38, 3], and KDEy-ML (hereafter KDEy(Gau)), since it uses Gaussian kernels [35], together with our proposed geometry-aware point estimator KDEy(Ait- λ). For uncertainty quantification, we include Bayes-ACC (the Bayesian adaptation of BBSE/ACC by [47]), Bayes-EMQ (aka MAPLS [46])⁴, Bayes-KDEy(Gau) (our Bayesian adaptation of KDEy), and Bayes-KDEy(Ait- λ) (our proposed Bayesian geometry-aware KDE), with Bootstrap variants of CC (Boots-CC) and PCC (Boots-PCC) as naive baselines. We exclude Precise Quantifier [26], since it is binary-only. To the best of our knowledge, no additional Bayesian implementations are available for multiclass quantification. We use the implementations of baseline methods available in QuaPy [34]. The code that reproduces our experiments is available online⁵.

Protocol. Evaluation follows a Dirichlet-sampling protocol [3]: for each dataset, we extract 500 test bags satisfying prevalence vectors sampled from a Dirichlet(α) on the simplex, thereby simulating label shift. Following [3], we use $\alpha = 1$ to generate a uniform coverage of the simplex,⁶ $\alpha = 0.1$ to generate prevalence samples from the border, and $\alpha = 10$ to generate samples concentrated on the center of the simplex. Bag size depends on the dataset and ranges from 100 (Twitter data) to 2000 (CIFAR100); full details are given in Appendix D.1.

Evaluation metrics. Point-estimation performance is evaluated in terms of absolute error $AE(\pi, \hat{\pi}) = K^{-1} \|\pi - \hat{\pi}\|_1$, and the squared weight-ratio error $W(\pi, \hat{\pi}) = K^{-1} \|w - \hat{w}\|_2^2$, with $w_i = \pi_i / \pi_i^{\text{train}}$, and $\hat{w}_i = \hat{\pi}_i / \pi_i^{\text{train}}$. AE is arguably the most directly interpretable measure of prevalence estimation error [40], while W is particularly informative when prevalence estimates are used to construct class-wise importance weights for domain adaptation via importance-weighted empirical risk minimization [31, 4, 3]. For Bayesian methods, posterior inference is performed with NUTS [23] using 500 warmup steps, and point-estimation metrics are computed from the posterior mean of the 1000 sampled prevalence vectors. Unless explicitly stated, we consider no pre-experimental knowledge, therefore employing a uniform prior. Uncertainty is evaluated in terms of coverage and amplitude over the empirical classwise confidence intervals $\mathcal{C} = \{[\ell_k, u_k]\}_{k=1}^K$ constructed at 95% level. Concretely, we report standard (hard) coverage (h-Cov) as the proportion of experiments in which the true prevalence values are simultaneously contained in their respective Bonferroni-corrected confidence intervals; soft coverage (s-Cov) as the proportion of prevalence values included in their corresponding (uncorrected) confidence intervals; and amplitude (Amp) as the mean percentage of the simplex volume (as estimated via Monte Carlo sampling) covered by the hyper-rectangle induced by the classwise intervals. For coverage (h-Cov, s-Cov), we report the gap with respect to the nominal value 95%, so that lower is better for all the metrics we report.

Model selection and calibration. Classifier hyperparameters are treated as quantifier hyperparameters and selected by minimizing absolute error (AE) on 100 bags generated using the Dirichlet($\alpha = 1$) sampling protocol from a held-out stratified validation split (40% of the training data). Quantifier-specific hyperparameters include kernel bandwidths

²LeQua2022: <https://doi.org/10.5281/zenodo.5734464> LeQua2024: <https://doi.org/10.5281/zenodo.10654474>

³https://zenodo.org/record/4255764/files/tweet_sentiment_quantification_snam.zip

⁴We adapted the original code https://github.com/ChangkunYe/MAPLS/blob/main/label_shift/mapls.py

⁵<https://github.com/AlexMoreo/BayesKDEy>

⁶This is equivalent to the so-called Artificial Prevalence Protocol (APP) in the quantification literature [16].

Table 1: Point-estimation summary by modality in terms of average rank (lower is better).

Method	AE rank				W rank			
	tabular	text	image	avg	tabular	text	image	avg
CC [16]	4.4	4.9	4.8	4.6	4.5	4.4	5.2	4.5
PCC [16]	5.5	5.9	6.0	5.7	5.4	5.6	5.8	5.5
BBSE/ACC [31]	4.1	4.1	4.2	4.1	3.9	4.3	4.0	4.0
MLLS/EMQ [38, 3]	2.8	2.3	2.0	2.5	2.8	2.1	2.2	2.5
KDEy(Gau) [35]	2.4	1.9	2.4	2.2	2.4	2.1	2.4	2.3
KDEy(Ait- λ) (ours)	1.9	1.9	1.6	1.9	2.1	2.5	1.4	2.2

Table 2: Bayesian uncertainty-aware quantification summary. AE and W ranks are reported for the $T = 1$ setting only. Coverage gaps and amplitudes are shown as mean \pm standard deviation across datasets, both for $T = 1$ and for temperature-calibrated models.

Method	AE rank	W rank	Temperature = 1			Calibrated		
			h-Cov gap	s-Cov gap	amp	h-Cov gap	s-Cov gap	amp
Boots-CC (baseline)	4.6	4.5	60.5 \pm 30.8	39.3 \pm 28.1	1.7 \pm 2.8	—	—	—
Boots-PCC (baseline)	5.6	5.5	74.5 \pm 24.0	52.4 \pm 30.3	1.2 \pm 2.1	—	—	—
Bayes-ACC [47]	3.9	3.9	13.3 \pm 21.7	4.4 \pm 8.3	5.4 \pm 7.3	18.5 \pm 23.4	7.1 \pm 11.5	6.6 \pm 10.6
Bayes-EMQ (MAPLS) [46]	2.9	2.6	25.3 \pm 30.2	10.9 \pm 14.9	3.0 \pm 4.2	19.5 \pm 22.8	6.0 \pm 7.5	4.5 \pm 7.9
Bayes-KDEy(Gau) (new)	2.1	2.5	20.3 \pm 30.1	7.3 \pm 14.4	3.6 \pm 5.4	12.9 \pm 18.0	3.1 \pm 5.6	5.2 \pm 7.6
Bayes-KDEy(Ait- λ) (ours)	1.9	2.1	21.7 \pm 31.1	7.9 \pm 14.1	3.6 \pm 5.4	12.9 \pm 18.6	3.3 \pm 6.1	6.4 \pm 11.4

and the shrinkage parameter λ . For Bayesian methods, posterior temperature is then *post hoc* calibrated on the same validation bags by minimizing the mean classwise Winkler’s interval score [19]. Full grids are reported in Appendix D.2.

6.1 Results

Point estimation. Table 1 summarizes point-estimation performance using average ranks for AE and W, reported by modality and overall, for the Dirichlet($\alpha = 1$) sampling protocol. Average ranks are preferable here because raw error scales differ substantially across datasets; full tables with raw values are given in Appendix D.3. The geometry-aware KDE is fully competitive in the point-estimation regime and typically improves over Gaussian KDE. Overall, KDEy(Ait- λ) achieves the best average rank in both AE and W, with especially strong results on tabular and image datasets.

Uncertainty evaluation. Table 2 summarizes Bayesian results for uncertainty-aware quantification; full tables with raw values are given in Appendix D.4. In our experiments, temperature calibration mainly affects uncertainty rather than the posterior mean, and does not change the overall ranking. For this reason, we report AE and W ranks for the untempered posterior ($T = 1$), while coverage gaps and amplitude are shown for both $T = 1$ and the temperature-calibrated setting. For coverage, we report the absolute deviation from the nominal 95% level, so lower values are better. In the untempered regime, Bayes-KDEy(Ait- λ) achieves the best aggregate AE and W ranks, closely followed by Bayes-KDEy(Gau). Bootstrap baselines yield very small amplitudes but poor coverage, making them unreliable as uncertainty quantifiers. Bayes-ACC attains the best raw coverage gaps at $T = 1$, but at the cost of substantially larger regions and clearly weaker point-estimation performance. Bayes-EMQ offers a stronger trade-off, yet both KDE-based Bayesian models remain better overall in aggregate ranking. As expected, temperature calibration reduces coverage gaps at the cost of amplitude for most methods (but Bayes-ACC). After calibration, the KDE-based Bayesian methods offer the best coverage, while Bayes-EMQ has the smallest amplitude.

Levels of shift. Figure 3 shows performance variation as a function of the severity of label shift. In this experiment, shift magnitude is measured in terms of $\|\pi - \pi^{\text{train}}\|_1$, and the tests are partitioned into three quantile-based groups, corresponding to low-, medium-, and high-shift regimes with approximately the same number of experiments. AE ranks and standard deviations are computed at the micro-level within each group. This plot reveals our method tends to dominate across levels of shift and data modalities, with the sole exception of the text modality in the low-shift and medium-shift regimes, where Bayes-EMQ and Bayes-KDEy(Gau), respectively, show superior performance.

Target prevalence distributions. Following the experiments of [3], we analyze quantification performance under differently distributed target prevalences as generated from symmetric Dirichlet distributions with $\alpha_{\text{test}} \in \{0.1, 10\}$; see Figure 4. These settings favor prevalences near the simplex boundary and prevalences concentrated near the barycenter,

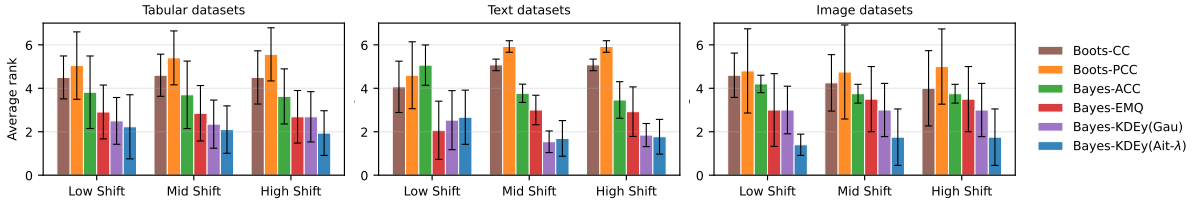


Figure 3: Average AE ranks in low-, medium-, and high-shift regimes for the three data modalities.

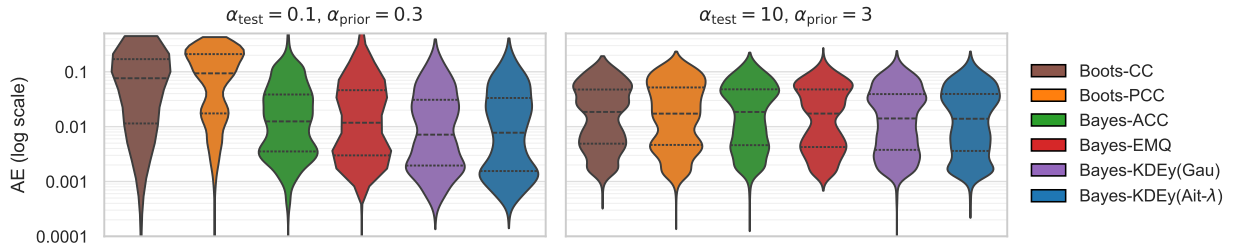


Figure 4: Violin plots for AE score distributions (log scale) for different target distributions.

respectively.⁷ Unlike [3], for Bayesian methods we additionally use informative but conservative symmetric Dirichlet priors, setting $\alpha_{\text{prior}} = 0.3$ for $\alpha_{\text{test}} = 0.1$ and $\alpha_{\text{prior}} = 3$ for $\alpha_{\text{test}} = 10$, effectively showcasing one of the main advantages of Bayesian inference. Results are by and large similar across methods for $\alpha_{\text{test}} = 10$, including bootstrap variants that cannot benefit from prior information, suggesting that bags concentrated near the simplex center are comparatively easier to quantify. The most informative case is $\alpha_{\text{test}} = 0.1$, where target prevalences lie near the simplex boundary and the task becomes more challenging. In this regime, bootstrap baselines degrade substantially, while Bayesian methods benefit from prior information. The shrinkage-regularized Aitchison KDE outperforms the Euclidean Gaussian KDE in this setting, where the target prevalence vector lies near the simplex boundary and geometric mismatch is expected to be most consequential. By respecting the simplex geometry, our method eliminates probability mass leakage outside valid bounds and provides higher resolution near the simplex boundaries, allowing for more precise estimation in this regime.

Ablation experiments. A naive Aitchison variant without shrinkage is reported in Appendix D.5. While competitive on many datasets, it exhibits sharp failures on a small but important set of benchmarks, namely LeQua2022-T1B, LeQua2024-T2, isolet, mhr, and wine-quality. In these cases, the pure Aitchison kernel (akin to $\lambda = 0$) yields substantially larger AE/W errors than the Gaussian variant. Importantly, these failures are largely removed by shrinkage, which brings the regularized Aitchison variant back to the range of the strongest competitors and, in most of these cases, above Gaussian KDE. More generally, the shrinkage values chosen during model selection are far from uniform across the 42 datasets: a near-pure Aitchison regime ($\lambda = 0.001$) is the most frequently selected setting, occurring in 31.0% of the cases, while a near-Gaussian regime ($\lambda = 0.999$) is the second most frequent, occurring in 16.7% of the cases. This indicates that shrinkage is not merely acting as a numerical safeguard, but as an adaptive mechanism that selects the geometry most compatible with the posterior structure of each dataset.

Computational cost. The proposed method requires the bandwidth and shrinkage to be optimized, which increases the computational cost. However, once set, the cost at inference time is not significantly different from that of the competitors. All experiments were run on a standard desktop workstation, without requiring specialized high-performance computing infrastructure.

Statistical significance. Pairwise significance was assessed at the dataset level using paired Wilcoxon signed-rank tests with Holm–Bonferroni correction after averaging results across bags within each dataset; see Appendix D.3 and D.4. The proposed method consistently belongs to the top statistical group. In the point-estimation regime, it significantly improves over CC, PCC, and BBSE/ACC ($p < 0.001$) and over MLLS/EMQ ($p < 0.05$), while remaining statistically indistinguishable from KDEy(Gau). In the Bayesian regime at $T = 1$, KDEy(Ait- λ) significantly improves over the bootstrap baselines, Bayes-ACC, and Bayes-EMQ (MAPLS) ($p < 0.001$), while remaining statistically tied with its Gaussian KDE analogue within the Bayesian formulation developed in this paper. The same pattern holds after temperature calibration.

⁷The LeQua datasets are not included in this experiment, since the test bags are fixed and do not contain per-instance labels.

7 Conclusions

We have presented a geometry-aware, uncertainty-aware approach to multiclass quantification under label shift. The method is based on two ideas. First, we revisit KDE-based quantification through compositional data analysis, replacing Euclidean density estimation on posterior probabilities with a shrinkage-regularized log-ratio representation better aligned with simplex geometry. Second, we show that this density model admits a Bayesian formulation, enabling posterior inference over class prevalences and principled uncertainty quantification. Empirically, the proposed geometry-aware KDE often outperforms standard Gaussian KDE and other baselines in both point estimation and uncertainty quantification. These results suggest that respecting simplex geometry is not only well motivated, but also practically beneficial for multiclass quantification. Our experiments also show that geometry-awareness alone is not sufficient: shrinkage is central to stabilizing log-ratio modeling near the simplex boundary.

Limitations and open directions: Our investigation is limited to the case in which the shrinkage and bandwidth values are selected by validation, while a fuller Bayesian treatment of these parameters may be worth investigating. Our method strongly relies on the distributional assumptions characteristics of label shift. Studying variants for different types of shift such as covariate shift [43] or sparse joint shift [7], appears to be a promising direction for future work in quantification.

References

- [1] John Aitchison. The statistical analysis of compositional data. *Journal of the Royal Statistical Society: Series B (Methodological)*, 44(2):139–160, 1982.
- [2] John Aitchison and Ian J Lauder. Kernel density estimation for compositional data. *Journal of the Royal Statistical Society: Series C (Applied Statistics)*, 34(2):129–137, 1985.
- [3] Amr Alexandari, Anshul Kundaje, and Avanti Shrikumar. Maximum likelihood with bias-corrected calibration is hard-to-beat at label shift adaptation. In *Proceedings of the 37th International Conference on Machine Learning (ICML 2020)*, pages 222–232, Virtual Event, 2020.
- [4] Kamyar Aizzadenesheli, Anqi Liu, Fanny Yang, and Animashree Anandkumar. Regularized learning for domain adaptation under label shifts. In *Proceedings of the 7th International Conference on Learning Representations (ICLR 2019)*, New Orleans, US, 2019.
- [5] Alberto Castaño, Pablo González, Jaime A. González, and Juan J. del Coz. Matching distributions algorithms based on the Earth Mover’s Distance for ordinal quantification. *IEEE Transactions On Neural Networks and Learning Systems*, 2022. Forthcoming.
- [6] José E Chacón, G Mateu-Figuera, and Josep-Antoni Martín-Fernández. Gaussian kernels for density estimation with compositional data. *Computers & Geosciences*, 37(5):702–711, 2011.
- [7] Lingjiao Chen, Matei Zaharia, and James Y Zou. Estimating and explaining model performance when both covariates and labels shift. *Advances in Neural Information Processing Systems*, 35:11467–11479, 2022.
- [8] Clemens Damke and Eyke Hüllermeier. Distribution matching for graph quantification under structural covariate shift. In *Joint European Conference on Machine Learning and Knowledge Discovery in Databases*, pages 403–419. Springer, 2025.
- [9] Ashlynn R. Daughton and Michael J. Paul. Constructing accurate confidence intervals when aggregating social media data for public health monitoring. In *Proceedings of the 3rd AAAI International Workshop on Health Intelligence (W3PHIAI 2019)*, pages 9–17, Phoenix, US, 2019.
- [10] Benjamin Denham, Edmund MK Lai, Roopak Sinha, and M Asif Naeem. Gain-some-lose-some: Reliable quantification under general dataset shift. In *2021 IEEE International Conference on Data Mining (ICDM)*, pages 1048–1053. IEEE, 2021.
- [11] Bastien Dussap, Gilles Blanchard, and Badr-Eddine Chérif-Abdellatif. Label shift quantification with robustness guarantees via distribution feature matching. In *Proceedings of the 34th European Conference on Machine Learning and Principles and Practice of Knowledge Discovery in Databases (ECML / PKDD 2023)*, pages 69–85, Torino, IT, 2023.
- [12] Andrea Esuli, Alejandro Moreo, and Fabrizio Sebastiani. LeQua@CLEF 2022: Learning to quantify. In *European Conference on Information Retrieval*, pages 374–381. Springer, 2022.
- [13] Andrea Esuli, Alejandro Moreo, Fabrizio Sebastiani, and Gianluca Sperduti. An overview of LeQua 2024, the 2nd international data challenge on learning to quantify. In *4th International Workshop on Learning to Quantify (LQ 2024)*, page 51, 2024.

- [14] Afonso Fernandes Vaz, Rafael Izbicki, and Rafael Bassi Stern. Quantification under prior probability shift: The ratio estimator and its extensions. *Journal of Machine Learning Research*, 20:79:1–79:33, 2019.
- [15] Jacob Fiksel, Abhirup Datta, Agbessi Amouzou, and Scott Zeger. Generalized Bayes quantification learning under dataset shift. *Journal of the American Statistical Association*, 117(540):2163–2181, 2022.
- [16] George Forman. Counting positives accurately despite inaccurate classification. In *Proceedings of the 16th European Conference on Machine Learning (ECML 2005)*, pages 564–575, Porto, PT, 2005.
- [17] Wei Gao and Fabrizio Sebastiani. From classification to quantification in Tweet sentiment analysis. *Social Network Analysis and Mining*, 6(1):19, 2016.
- [18] Saurabh Garg, Yifan Wu, Sivaraman Balakrishnan, and Zachary Lipton. A unified view of label shift estimation. In *Proceedings of the 34th Conference on Neural Information Processing Systems (NeurIPS 2020)*, pages 3290–3300, Virtual Event, 2020.
- [19] Tilmann Gneiting and Adrian E Raftery. Strictly proper scoring rules, prediction, and estimation. *Journal of the American statistical Association*, 102(477):359–378, 2007.
- [20] Patrick Godau, Piotr Kalinowski, Evangelia Christodoulou, Annika Reinke, Minu Tizabi, Luciana Ferrer, Paul Jäger, and Lena Maier-Hein. Navigating prevalence shifts in image analysis algorithm deployment. *Medical image analysis*, page 103504, 2025.
- [21] Víctor González-Castro, Rocío Alaiz-Rodríguez, and Enrique Alegre. Class distribution estimation based on the Hellinger distance. *Information Sciences*, 218:146–164, 2013.
- [22] Chuan Guo, Geoff Pleiss, Yu Sun, and Kilian Q Weinberger. On calibration of modern neural networks. In *International conference on machine learning*, pages 1321–1330. PMLR, 2017.
- [23] Matthew D Hoffman, Andrew Gelman, et al. The No-U-Turn sampler: adaptively setting path lengths in hamiltonian monte carlo. *J. Mach. Learn. Res.*, 15(1):1593–1623, 2014.
- [24] Daniel J. Hopkins and Gary King. A method of automated nonparametric content analysis for social science. *American Journal of Political Science*, 54(1):229–247, 2010.
- [25] Jiawei Hu and Javier A Barria. Bayesian-based online label shift estimation with dynamic Dirichlet priors. *arXiv preprint arXiv:2511.18615*, 2025.
- [26] Aime Bienfait Igiraneza, Christophe Fraser, and Robert Hinch. Estimating prevalence with precision and accuracy. *arXiv preprint arXiv:2507.06061*, 2025.
- [27] Thomas Jaenich, Alejandro Moreo, Alessandro Fabris, Graham McDonald, Andrea Esuli, Iadh Ounis, and Fabrizio Sebastiani. Quantifying query fairness under unawareness. *Journal of Artificial Intelligence Research*, 85, 2026.
- [28] Markelle Kelly, Rachel Longjohn, and Kolby Nottingham. The UCI machine learning repository. <https://archive.ics.uci.edu>.
- [29] Alex Krizhevsky and Geoffrey Hinton. Learning multiple layers of features from tiny images. Technical report, University of Toronto, Toronto, Ontario, 2009.
- [30] Yann LeCun, Corinna Cortes, and Christopher J. C. Burges. The MNIST database of handwritten digits. <http://yann.lecun.com/exdb/mnist/>, 1998.
- [31] Zachary C. Lipton, Yu-Xiang Wang, and Alexander J. Smola. Detecting and correcting for label shift with black box predictors. In *Proceedings of the 35th International Conference on Machine Learning (ICML 2018)*, pages 3128–3136, Stockholm, SE, 2018.
- [32] JA Martín-Fernández, JE Chacón, and G Mateu-Figueras. Updating on the kernel density estimation for compositional data. In *of: Proceedings of the 17th Conference IASC-ERSS, Compstat, Roma,(Italy)*, pages 713–720, 2006.
- [33] Alessio Micheli, Alejandro Moreo, Marco Podda, Fabrizio Sebastiani, William Simoni, and Domenico Tortorella. Efficient quantification on large-scale networks. *Machine Learning*, 114(12):1–26, 2025.
- [34] Alejandro Moreo, Andrea Esuli, and Fabrizio Sebastiani. QuaPy: a Python-based framework for quantification. In *Proceedings of the 30th ACM International Conference on Information & Knowledge Management*, pages 4534–4543, 2021.
- [35] Alejandro Moreo, Pablo González, and Juan José del Coz. Kernel density estimation for multiclass quantification. *Machine Learning*, 114(4), 2025.
- [36] Yuval Netzer, Tao Wang, Adam Coates, Alessandro Bissacco, Baolin Wu, Andrew Y Ng, et al. Reading digits in natural images with unsupervised feature learning. In *NIPS workshop on deep learning and unsupervised feature learning*, volume 2011, page 4. Granada, 2011.

- [37] Frédéric Ouimet and Raimon Tolosana-Delgado. Asymptotic properties of Dirichlet kernel density estimators. *Journal of Multivariate Analysis*, 187:104832, 2022.
- [38] Marco Saerens, Patrice Latinne, and Christine Decaestecker. Adjusting the outputs of a classifier to new a priori probabilities: A simple procedure. *Neural Computation*, 14(1):21–41, 2002.
- [39] Tobias Schumacher, Markus Strohmaier, and Florian Lemmerich. A comparative evaluation of quantification methods. *Journal of Machine Learning Research*, 26(55):1–54, 2025.
- [40] Fabrizio Sebastiani. Evaluation measures for quantification: An axiomatic approach. *Information Retrieval Journal*, 23(3):255–288, 2020.
- [41] Amos Storkey. When training and test sets are different: Characterizing learning transfer. In Joaquin Quiñero-Candela, Masashi Sugiyama, Anton Schwaighofer, and Neil D. Lawrence, editors, *Dataset shift in machine learning*, pages 3–28. The MIT Press, Cambridge, US, 2009.
- [42] Dirk Tasche. Confidence intervals for class prevalences under prior probability shift. *Machine Learning and Knowledge Extraction*, 1(3):805–831, 2019.
- [43] Dirk Tasche. Class prior estimation under covariate shift: No problem? *arXiv preprint arXiv:2206.02449*, 2022.
- [44] Lorenzo Volpi, Alejandro Moreo, and Fabrizio Sebastiani. LEAP: Linear equations for classifier accuracy prediction under prior probability shift. *Machine Learning*, 114(12):293, 2025.
- [45] Han Xiao, Kashif Rasul, and Roland Vollgraf. Fashion-MNIST: a novel image dataset for benchmarking machine learning algorithms. *arXiv preprint arXiv:1708.07747*, 2017.
- [46] Changkun Ye, Russell Tsuchida, Lars Petersson, and Nick Barnes. Label shift estimation for class-imbalance problem: A Bayesian approach. In *Proceedings of the IEEE/CVF winter conference on applications of computer vision*, pages 1073–1082, 2024.
- [47] Albert Ziegler and Paweł Czyż. Bayesian quantification with black-box estimators. *Transactions on Machine Learning Research*, 2024.

Appendix

A Proof of Proposition 1: linearization of CLR through shrinkage

In this appendix we prove the local linearization result stated in the main text. Throughout the proof, we let $\phi = \text{CLR}$. *Proposition 2.* Let $u = (\frac{1}{K}, \dots, \frac{1}{K})$ be the barycenter of the simplex Δ^{K-1} , and define the shrinkage operator

$$T_\lambda(p) = (1 - \lambda)p + \lambda u, \quad \lambda \in [0, 1).$$

For any fixed $p \in \Delta^{K-1, \circ}$, it holds that

$$\phi(T_\lambda(p)) = K(1 - \lambda)(p - u) + O((1 - \lambda)^2) \quad \text{as } \lambda \rightarrow 1.$$

Proof. The shrinkage operator can be written as

$$T_\lambda(p) = u + \varepsilon \delta,$$

with $\delta := p - u$, $\varepsilon := 1 - \lambda$. Since both p and u belong to the simplex, it is implied that $\sum_{i=1}^K \delta_i = 0$. Note that each component of $T_\lambda(p)$ can be written as

$$[T_\lambda(p)]_i = \frac{1}{K} + \varepsilon \delta_i.$$

Because $p \in \Delta^{K-1, \circ}$, all its coordinates are strictly positive. Hence, for λ sufficiently close to 1 (equivalently, ε sufficiently small), all coordinates of $T_\lambda(p)$ remain strictly positive as well.

By definition of the CLR map,

$$[\phi(T_\lambda(p))]_i = \log([T_\lambda(p)]_i) - \frac{1}{K} \sum_{j=1}^K \log([T_\lambda(p)]_j). \quad (4)$$

We start with the first term of Equation 4, and expand the logarithm around the simplex barycenter. For each $i \in \{1, \dots, K\}$,

$$\log([T_\lambda(p)]_i) = \log\left(\frac{1}{K} + \varepsilon \delta_i\right) = \log \frac{1}{K} + \log(1 + K\varepsilon \delta_i).$$

Using the second-order Taylor expansion $\log(1 + x) = x - \frac{x^2}{2} + O(x^3)$, for $x = K\varepsilon \delta_i$ in the right-hand term, we obtain

$$\log([T_\lambda(p)]_i) = \log \frac{1}{K} + K\varepsilon \delta_i - \frac{K^2 \varepsilon^2}{2} \delta_i^2 + O(\varepsilon^3 \|\delta\|^3). \quad (5)$$

For the second term of Equation 4, we need to average over the log coordinates in Equation 5. This yields

$$\frac{1}{K} \sum_{j=1}^K \log([T_\lambda(p)]_j) = \log \frac{1}{K} + K\varepsilon \frac{1}{K} \sum_{j=1}^K \delta_j - \frac{K^2 \varepsilon^2}{2} \frac{1}{K} \sum_{j=1}^K \delta_j^2 + O(\varepsilon^3 \|\delta\|^3).$$

Since $\sum_{j=1}^K \delta_j = 0$, this simplifies to

$$\frac{1}{K} \sum_{j=1}^K \log([T_\lambda(p)]_j) = \log \frac{1}{K} - \frac{K\varepsilon^2}{2} \sum_{j=1}^K \delta_j^2 + O(\varepsilon^3 \|\delta\|^3). \quad (6)$$

For the complete derivation of the CLR map (Equation 4), we need to subtract the two expansions above (Equations 5 and 6); this gives

$$\begin{aligned} [\phi(T_\lambda(p))]_i &= K\varepsilon \delta_i - \frac{K^2 \varepsilon^2}{2} \delta_i^2 + \frac{K\varepsilon^2}{2} \sum_{j=1}^K \delta_j^2 + O(\varepsilon^3 \|\delta\|^3) \\ &= K\varepsilon \delta_i + O(\varepsilon^2 \|\delta\|^2). \end{aligned}$$

Since this holds componentwise, we can write in vector form

$$\phi(T_\lambda(p)) = K\varepsilon\delta + O(\varepsilon^2\|\delta\|^2).$$

Recalling that $\varepsilon = 1 - \lambda$ and $\delta = p - u$, we obtain

$$\phi(T_\lambda(p)) = K(1 - \lambda)(p - u) + O((1 - \lambda)^2\|p - u\|^2),$$

which proves the first claim. The weaker bound

$$\phi(T_\lambda(p)) = K(1 - \lambda)(p - u) + O((1 - \lambda)^2)$$

follows immediately for fixed p . □

Remark 2. The proposition shows that shrinkage does not remove the compositional structure of the problem. Rather, it moves posterior vectors towards a regime where the log-ratio map is locally well approximated by a linear transformation. In this sense, shrinkage regularizes the most nonlinear part of the simplex geometry, namely the neighborhood of the boundary.

B Bandwidth scaling under shrinkage

The regularization of the log-ratio coordinates in our model is achieved by a shrinkage operator that effectively reduces the operational region of the density model in the simplex. In order to preserve coherence with a set of reference bandwidth values (e.g., a grid of values to be explored under model selection), the kernel bandwidths have to be transformed consequentially. In this appendix we justify the bandwidth rescaling used in the main text. Recall the shrinkage map

$$T_\lambda(p) = (1 - \lambda)p + \lambda u, \quad \lambda \in [0, 1),$$

where $u = (\frac{1}{K}, \dots, \frac{1}{K})$ is the barycenter of the simplex Δ^{K-1} . Let $d = K - 1$ denote the intrinsic dimension of the simplex.

Proposition 3. Under the shrinkage map T_λ , the natural scaling of a reference bandwidth h is

$$h_{\text{eff}} = (1 - \lambda)h.$$

Moreover, if a density is normalized with respect to the simplex volume measure, then its height rescales by the Jacobian factor $(1 - \lambda)^{-d}$.

Proof. The map T_λ is affine, and for any two simplex points $p, q \in \Delta^{K-1}$,

$$T_\lambda(p) - T_\lambda(q) = (1 - \lambda)(p - q).$$

Hence all Euclidean distances in the affine hyperplane containing the simplex are uniformly contracted by the factor $a = 1 - \lambda$.

Now consider an isotropic Gaussian kernel centered at some point c in the simplex hyperplane,

$$\mathcal{K}_h(p - c) \propto \exp\left(-\frac{\|p - c\|^2}{2h^2}\right).$$

After shrinkage, the corresponding point is $p' = T_\lambda(p)$, and similarly the center is mapped to $c' = T_\lambda(c)$. Since T_λ is affine,

$$p' - c' = (1 - \lambda)(p - c),$$

so that

$$\|p' - c'\| = (1 - \lambda)\|p - c\|.$$

If we want the kernel to preserve the same relative spread with respect to the contracted simplex, then the normalized distance should remain unchanged, i.e.,

$$\frac{\|p' - c'\|}{h_{\text{eff}}} = \frac{\|p - c\|}{h}.$$

Substituting $\|p' - c'\| = (1 - \lambda)\|p - c\|$, we obtain

$$\frac{(1 - \lambda)\|p - c\|}{h_{\text{eff}}} = \frac{\|p - c\|}{h},$$

which implies

$$h_{\text{eff}} = (1 - \lambda)h.$$

To derive the density scaling, note that T_λ acts on a d -dimensional affine subspace, with $d = K - 1$. Since the map is a uniform contraction by factor $1 - \lambda$, its Jacobian determinant on this subspace is $(1 - \lambda)^d$. Therefore, if a density is normalized with respect to the simplex volume measure, then under change of variables its height must be multiplied by $(1 - \lambda)^{-d}$ in order to preserve total probability mass. \square

Remark 3 (Discarding Jacobian scaling). For fixed λ , the Jacobian factor $(1 - \lambda)^{-d}$ is a constant multiplicative term shared by all kernels and all class-conditional densities. It therefore factors out of the mixture in Equation 2 and is independent of π . Consequently, it only adds a constant to the log-likelihood in Equation 1 and only changes the posterior normalization in Equation 3. For fixed λ it may thus be omitted for inference with respect to π .

Remark 4 (Connection with the CLR geometry). The previous proposition is stated in the simplex hyperplane. In the main text, however, density estimation is performed after the log-ratio transformation ϕ . The local linearization result of Proposition 1 shows that, near the simplex barycenter,

$$\phi(T_\lambda(p)) = K(1 - \lambda)(p - u) + O((1 - \lambda)^2 \|p - u\|^2).$$

Thus, to first order, shrinkage also contracts distances in CLR coordinates by the same factor $1 - \lambda$. This justifies using the same bandwidth rescaling rule in the transformed space:

$$h_{\text{eff}} = (1 - \lambda)h.$$

In other words, shrinkage not only regularizes the geometry, but also induces a natural linear rescaling of the kernel bandwidth.

C Estimator-level effects of shrinkage

In this appendix we provide a heuristic interpretation of the effect of shrinkage at the level of the KDE estimator. The goal is not to establish a full estimator equivalence, but to explain why shrinkage moves the geometry-aware estimator into a locally Euclidean regime near the simplex barycenter.

Let Δ^{K-1} be the probability simplex, let u denote its barycenter, and let

$$T_\lambda(p) = (1 - \lambda)p + \lambda u$$

be the shrinkage map. Let $\phi = \text{CLR}$, and let

$$\mathcal{P}^* = \{p^{(1)}, \dots, p^{(n)}\} \subset \Delta^{K-1}$$

be a set of reference posterior vectors. For $d = K - 1$, define the Gaussian kernel on the simplex hyperplane by

$$\mathcal{K}_b(r) = (2\pi b^2)^{-d/2} \exp\left(-\frac{\|r\|^2}{2b^2}\right).$$

Consider the transformed-space KDE

$$\hat{f}_{\lambda,h}^{\text{tr}}(p) = \frac{1}{n} \sum_{i=1}^n \mathcal{K}_h\left(\phi(T_\lambda(p)) - \phi(T_\lambda(p^{(i)}))\right).$$

Remark 5 (Heuristic local Euclidean regime induced by shrinkage). Assume that p and all reference points $p^{(i)}$ lie in a sufficiently small neighborhood of the barycenter. By the local linearization result of Appendix A,

$$\phi(T_\lambda(p)) - \phi(T_\lambda(p^{(i)})) = K(1 - \lambda)(p - p^{(i)}) + r_i(p),$$

where the remainder $r_i(p)$ is of higher order in the local displacement from u .

Now set

$$h_{\text{eff}} = (1 - \lambda)h.$$

Substituting the linear term into the Gaussian kernel yields

$$\mathcal{K}_{h_{\text{eff}}}\left(K(1 - \lambda)(p - p^{(i)})\right) = C_{\lambda,K} \mathcal{K}_{h/K}\left(p - p^{(i)}\right),$$

where

$$C_{\lambda,K} = (K(1 - \lambda))^{-(K-1)}$$

is a multiplicative constant independent of p . A first-order Taylor expansion of $\mathcal{K}_{h_{\text{eff}}}$ around the linear term therefore gives

$$\mathcal{K}_{h_{\text{eff}}}\left(\phi(T_\lambda(p)) - \phi(T_\lambda(p^{(i)}))\right) = C_{\lambda,K} \mathcal{K}_{h/K}\left(p - p^{(i)}\right) + \text{higher-order local terms.}$$

Averaging over i , one obtains the heuristic approximation

$$\hat{f}_{\lambda,h_{\text{eff}}}^{\text{tr}}(p) \approx C_{\lambda,K} \hat{f}_{h/K}^{\text{Euc}}(p),$$

where $\hat{f}_{h/K}^{\text{Euc}}$ denotes the Euclidean Gaussian KDE on the simplex hyperplane with bandwidth h/K .

Thus, shrinkage does not remove the compositional structure of the estimator, but places it in a regime where the induced smoothing is locally well approximated by Euclidean Gaussian smoothing. Since the factor $C_{\lambda,K}$ is independent of p , it contributes only an additive constant to the corresponding log-likelihood. Consequently, it does not affect maximum likelihood estimation or Bayesian inference with respect to the prevalence vector π .

The class-conditional estimators used in the main text are obtained by applying the same construction separately to the class-specific reference sets.

D Additional Experimental Details

D.1 Datasets

Dataset details are provided in Table 3. For the LeQua datasets, validation and test pool sizes are not reported because the data are provided directly as predefined bags rather than as instance-level pools from which bags are sampled. In our experiments, we use the first 100 validation bags and the first 500 test bags. For image datasets, the training and validation sizes reported in this table refer to the effective feature-level splits used for quantification, not to the original raw dataset splits. The representation model is first trained on 70% of the original training set and monitored on the remaining 30%. After training, features are extracted from that 30% split and from the original test set; the training/validation/test sizes reported here are defined on these extracted-feature splits.

D.2 Hyperparameter Grids and Model Selection

Classifier hyperparameters are treated as quantifier hyperparameters and are optimized using quantification-oriented validation loss. The hyperparameters we explore are specified in Table 4.

Hyperparameters are selected by minimizing the absolute error (AE) of the corresponding point estimator on 100 validation bags generated under a Dirichlet(1) sampling protocol. For Bayesian methods, we additionally perform *post hoc* temperature calibration after model selection. The temperature is searched over the grid $T \in \{\frac{1}{2}, 1, 1.5, 2, 5, 10, 100, 1000\}$, and selected by minimizing the mean Winkler score (aka interval score) [19] across classes on the same validation bags. Given classwise confidence intervals $\mathcal{C} = \{[\ell_k, u_k]\}_{k=1}^K$ constructed at significance level α , the mean Winkler score is defined as

$$\mathcal{W}(\pi, \mathcal{C}; \alpha) = \frac{1}{K} \sum_{k=1}^K \left[(u_k - \ell_k) + \frac{2}{\alpha} (\max(0, \ell_k - \pi_k) + \max(0, \pi_k - u_k)) \right]. \quad (7)$$

Table 3: Dataset details.

Dataset	Modality	Train	Val	Test	Bag size	Features	Classes
abalone	tabular	2,846	1,139	1,220	1,000	9	15
academic-success	tabular	3,096	1,239	1,328	1,000	36	3
chess	tabular	19,198	7,680	8,228	1,000	20	13
cmc	tabular	1,031	413	442	1,000	9	3
connect-4	tabular	25,000	10,000	42,557	1,000	84	3
digits	tabular	3,933	1,574	1,687	1,000	64	10
dry-bean	tabular	9,527	3,811	4,084	1,000	16	7
hand_digits	tabular	7,694	3,078	3,298	1,000	16	10
image_seg	tabular	1,617	647	693	1,000	19	7
isolet	tabular	5,457	2,183	2,340	1,000	617	26
letter	tabular	14,000	5,600	6,000	1,000	16	26
mhr	tabular	709	284	305	1,000	6	3
molecular	tabular	2,233	894	957	1,000	227	3
nursery	tabular	9,070	3,628	3,888	1,000	19	4
obesity	tabular	1,477	591	634	1,000	23	7
page_block	tabular	3,811	1,525	1,634	1,000	10	4
phishing	tabular	947	379	406	1,000	9	3
satellite	tabular	4,504	1,802	1,931	1,000	36	6
shuttle	tabular	25,000	10,000	32,756	1,000	7	3
waveform-v1	tabular	3,500	1,400	1,500	1,000	21	3
wine-quality	tabular	4,523	1,810	1,939	1,000	11	5
yeast	tabular	1,035	414	444	1,000	8	9
gasp	text	8,788	1,256	3,765	100	78,244	3
hcr	text	1,594	797	798	100	22,061	3
omd	text	1,839	263	787	100	19,385	3
sanders	text	2,155	308	923	100	23,980	3
semeval13	text	11,338	1,654	3,813	100	107,984	3
semeval14	text	11,338	1,654	1,853	100	107,984	3
semeval15	text	11,338	1,654	2,390	100	107,984	3
semeval16	text	8,000	2,000	2,000	100	76,387	3
sst	text	2,971	425	1,271	100	29,664	3
wa	text	2,184	312	936	100	23,745	3
wb	text	4,259	609	1,823	100	40,507	3
LeQua2022-T1A	text	5,000	—	—	250	300	2
LeQua2022-T1B	text	20,000	—	—	1,000	300	28
LeQua2024-T1	text	5,000	—	—	250	256	2
LeQua2024-T2	text	20,000	—	—	1,000	256	28
CIFAR100	image	9,000	6,000	10,000	2,000	100	100
CIFAR10	image	9,000	6,000	10,000	500	10	10
MNIST	image	10,800	7,200	10,000	500	10	10
FashionMNIST	image	10,800	7,200	10,000	500	10	10
SVHN	image	13,186	8,791	26,032	500	10	10

Table 4: Hyperparameter grids used in model selection.

Component	Hyperparameter	Grid
Logistic Regression	C	$\text{logspace}(-4, 4, 9)$
Logistic Regression	class_weight	{balanced, None}
Gaussian KDE	h	$\text{logspace}(-2, 0, 10)$
Aitchison KDE	h	$\text{logspace}(-1, 1, 10)$
Shrinkage	λ	{0.001, 0.25, 0.5, 0.75, 0.9, 0.999}

D.3 Full Tables: Performance of point-estimators.

Table 5 reports the full AE and W results for point-estimation performance. The table uses the following conventions: For each dataset and metric, the best result is highlighted in bold. Results that are *not* statistically significantly different from the best one according to a paired Wilcoxon signed-rank test at significance level 0.05 are marked with † symbol. In addition, cells are color-coded for ease of visualization, with more intense cells indicating lower (better) errors and lighter cells indicating higher (worse) errors. Statistical significance comparisons are reported in Table 6. Symbols denote pairwise Wilcoxon-Holm comparisons across datasets on AE: $\ll / <$ mean the row method is significantly better than the column method ($p < 0.001 / p < 0.05$), $\gg / >$ mean significantly worse, \approx means not significantly different, and = marks the diagonal.

Table 5: Point-estimation performance in terms of AE and W

	AE					W						
	CC	PCC	BBSE/ACC	MLLS/EMQ	KDEy(Gau)	KDEy(Ait- λ)	CC	PCC	BBSE/ACC	MLLS/EMQ	KDEy(Gau)	KDEy(Ait- λ)
tabular												
abalone	0.0450	0.0424	0.0966	0.0655	0.0496	0.0505	7.0645	6.2734	96.8502	15.7999	9.7935	9.8538
academic-success	0.0953	0.1211	0.0491	0.0260	0.0251	0.0236	0.2541	0.4139	0.0796	0.0231	0.0210	0.0188
chess	0.0413	0.0450	0.0409	0.0398	†0.0165	0.0163	1.9618	2.3372	1.1529	1.3512	0.3125	0.3878
cmc	0.1560	0.1778	0.1065	0.0973	†0.0937	0.0934	0.3903	0.4937	0.2123	0.1884	†0.1913	†0.1925
connect-4	0.1138	0.1468	0.0270	0.0301	†0.0205	0.0201	1.0574	1.6642	0.0742	0.1020	0.0412	0.0395
digits	0.0035	0.0045	0.0030	0.0023	0.0024	0.0016	0.0034	0.0045	0.0017	0.0012	0.0014	0.0006
dry-bean	0.0088	0.0122	0.0040	0.0032	0.0032	0.0030	0.0066	0.0131	0.0020	0.0012	0.0011	0.0010
hand_digits	0.0048	0.0063	0.0031	0.0023	0.0023	0.0016	0.0054	0.0092	0.0018	0.0010	0.0011	0.0006
image_seg	0.0063	0.0083	0.0090	0.0051	0.0041	0.0041	0.0098	0.0164	0.0114	0.0046	0.0033	0.0034
isolet	0.0021	0.0023	0.0018	0.0014	0.0014	0.0013	0.0077	0.0092	0.0051	0.0034	0.0029	0.0027
letter	0.0077	0.0108	0.0048	0.0043	0.0025	0.0014	0.0856	0.1631	0.0300	0.0253	0.0078	0.0025
mhr	0.1216	0.1444	0.1113	0.0549	0.0257	0.0340	0.2154	0.2776	0.1621	0.0443	0.0104	0.0164
molecular	0.0188	0.0388	0.0089	0.0071	0.0072	0.0068	0.0066	0.0294	0.0014	0.0013	0.0011	0.0011
nursery	0.0179	0.0265	0.0050	†0.0051	0.0061	0.0069	0.1206	0.2875	0.0139	0.0256	0.0703	0.0474
obesity	0.0070	0.0072	0.0095	0.0050	0.0084	0.0085	0.0059	0.0065	0.0102	0.0029	0.0092	0.0093
page_block	0.0141	0.0271	0.0217	0.0170	0.0194	0.0215	0.3355	1.4168	1.4289	0.5930	1.1913	1.5181
phishing	0.0953	0.1062	0.0553	0.0281	0.0221	0.0243	1.3672	1.4128	0.4169	0.1092	0.0717	0.0872
satellite	0.0231	0.0312	0.0111	0.0076	0.0070	0.0078	0.0767	0.1463	0.0194	0.0077	0.0059	0.0078
shuttle	0.0073	0.0093	0.0021	0.0054	0.0019	0.0018	0.0028	0.0043	0.0004	0.0014	0.0003	0.0002
waveform-v1	0.0416	0.0582	0.0250	0.0070	0.0102	†0.0073	0.0234	0.0436	0.0094	0.0007	0.0015	0.0008
wine-quality	0.0998	0.1144	0.0879	0.0714	0.1328	†0.0729	5.4520	7.6107	2.9600	1.6965	9.9969	3.8726
yeast	0.0539	0.0557	0.0561	0.0647	0.0449	0.0437	7.5748	6.3074	6.7092	11.1195	5.8082	5.0089
text												
gasp	0.0899	0.1199	0.0518	0.0415	0.0409	0.0397	0.6271	1.2881	0.1704	0.1001	0.1149	†0.1011
hcr	0.1265	0.1524	0.0962	†0.0811	0.0814	0.0793	0.3777	0.4836	0.2078	0.1610	†0.1737	†0.1635
ond	0.1062	0.1182	0.0901	0.0688	†0.0620	0.0618	0.1844	0.2356	0.1412	0.0876	0.0715	†0.0745
sanders	0.1114	0.1341	0.0587	†0.0470	0.0459	†0.0463	0.5178	0.6633	0.1318	0.0930	0.0839	0.0892
semeval13	0.1115	0.1365	0.0758	0.0739	0.0580	†0.0589	0.2692	0.5073	0.1111	0.1040	0.0642	†0.0658
semeval14	0.1038	0.1332	0.0668	0.0656	0.0560	†0.0568	0.2100	0.4723	0.0967	0.1070	0.0776	0.0818
semeval15	0.1253	0.1425	0.0958	†0.0865	0.0863	0.0913	0.2880	0.4533	0.1585	0.1124	0.1520	0.1715
semeval16	0.1389	0.1612	0.1891	0.1110	0.1370	0.1390	0.5124	0.6856	1.1685	0.4215	0.6520	0.6749
sst	0.1051	0.1352	0.0749	†0.0539	0.0541	0.0538	0.1687	0.2659	0.0904	†0.0487	0.0490	0.0484
wa	0.0783	0.0819	0.0517	0.0500	0.0425	†0.0432	0.0873	0.0938	0.0393	0.0370	0.0281	†0.0297
wb	0.0804	0.0799	0.0439	0.0333	0.0343	0.0346	0.1001	0.0990	0.0316	0.0183	0.0190	0.0194
LeQua2022-T1A	0.0933	0.1181	0.0314	†0.0240	0.0242	0.0234	0.1260	0.2024	0.0170	†0.0099	†0.0097	0.0093
LeQua2022-T1B	0.0140	0.0165	0.0130	†0.0119	0.0118	0.0118	91.1316	118.7259	121.7791	92.8496	109.3588	109.3062
LeQua2024-T1	0.0862	0.1167	0.0270	†0.0205	0.0204	†0.0206	0.1114	0.1978	0.0130	†0.0078	0.0078	†0.0079
LeQua2024-T2	0.0171	0.0190	0.0170	0.0137	0.0160	0.0156	137.5911	163.6366	231.3429	100.8582	186.1994	196.3228
image												
CIFAR100	0.0025	0.0028	0.0022	0.0016	0.0018	0.0017	0.1375	0.1695	0.1009	0.0576	0.0712	0.0643
CIFAR10	0.0065	0.0080	0.0044	0.0036	0.0038	†0.0036	0.0092	0.0127	0.0037	†0.0025	0.0027	0.0024
MNIST	0.0016	0.0018	0.0017	0.0012	0.0012	0.0011	0.0007	0.0006	0.0005	0.0003	0.0003	0.0003
fashionMNIST	0.0083	0.0103	0.0047	0.0041	0.0038	0.0038	0.0201	0.0274	0.0052	0.0041	0.0036	0.0036
SVHN	0.0098	0.0106	0.0061	0.0053	0.0049	0.0045	0.0235	0.0284	0.0091	0.0072	0.0060	0.0052
Rank	4.6	5.7	4.1	2.5	2.2	1.9	4.5	5.5	4.0	2.5	2.3	2.2

D.4 Full Tables: Performance of uncertainty-aware estimators.

Table 7 reports the full AE and W results for the point-estimation performance of Bayesian methods and bootstrap-based baselines. Notational conventions are as in Table 5.

Tables 8 and 9 report coverage (hard, h-Cov, and soft, s-Cov) and amplitude results for 95% posterior intervals constructed from the 1000 samples generated by each method, with and without temperature calibration. In Table 8, highlighted cells indicate coverage values within the range $95\% \pm 5\%$, whereas in Table 9, highlighted cells indicate

Table 6: Pairwise symbolic matrix of Wilcoxon-Holm comparisons on AE.

	CC	PCC	BBSE/ACC	MLLS/EMQ	KDEy(Gau)	KDEy(Ait- λ)
CC	=	\ll	\gg	\gg	\gg	\gg
PCC	\gg	=	\gg	\gg	\gg	\gg
BBSE/ACC	\ll	\ll	=	\gg	\gg	\gg
MLLS/EMQ	\ll	\ll	\ll	=	\approx	\gt
KDEy(Gau)	\ll	\ll	\ll	\approx	=	\approx
KDEy(Ait- λ)	\ll	\ll	\ll	$<$	\approx	=

amplitude values covering at most 5% of the total simplex volume. As expected, temperature calibration often improves coverage at the expense of larger amplitude. Since the temperature grid includes one value below the default $T = 1$, namely $T = \frac{1}{2}$, calibration may in a few cases (e.g., datasets *wa* and *wb*) lead to lower coverage and smaller amplitude. Bootstrap methods are unaffected by temperature calibration.

Statistical significance comparisons are reported in Table 10. Notational conventions are as in Table 6.

D.5 Ablation experiment: unregularized geometry-aware KDE

Table 11 reports the results of KDEy(Ait), the unregularized geometry-aware KDE variant without shrinkage regularization. The results show that, although the pure Aitchison-based model performs well on most datasets, it also exhibits a few severe failures (notably on *isolet*, *mhr*, *wine-quality*, *LeQua2022-T1B*, and *LeQua2024-T2*). These failures are effectively corrected by the regularized variant KDEy(Ait- λ). The remaining methods are included for reference, and the selected value of λ is reported in the last column. Notational conventions are as in Table 5.

Table 7: Point-estimation performance of Bayesian methods in terms of AE and W

	AE						W						
	Boots-CC	Boots-PCC	Bayes-ACC	Bayes-EMQ (MAPLS)	Bayes-KDEy(Gau)	Bayes-KDEy(Ait- λ)	Boots-CC	Boots-PCC	Bayes-ACC	Bayes-EMQ (MAPLS)	Bayes-KDEy(Gau)	Bayes-KDEy(Ait- λ)	
tabular	abalone	0.0450	0.0424	0.0888	0.0555	0.0489	0.0489	7.0638	6.2735	40.9764	13.5245	9.5851	9.5199
	academic-success	0.0953	0.1211	0.0457	0.0254	0.0244	0.0230	0.2542	0.4139	0.0698	0.0220	0.0199	0.0178
	chess	0.0413	0.0450	0.0280	0.0345	0.0155	0.0161	1.9621	2.3368	0.5852	1.1171	0.3102	0.3897
	cmc	0.1560	0.1778	0.0987	0.0945	0.0911	\dagger 0.0912	0.3902	0.4938	\dagger 0.1830	0.1808	\dagger 0.1850	\dagger 0.1872
	connect-4	0.1138	0.1468	0.0266	0.0284	0.0201	\dagger 0.0201	1.0574	1.6643	0.0710	0.0896	\dagger 0.0390	0.0388
	digits	0.0036	0.0045	0.0031	0.0025	0.0026	0.0018	0.0034	0.0046	0.0018	0.0013	0.0015	0.0007
	dry-bean	0.0088	0.0122	0.0042	0.0034	0.0034	0.0032	0.0066	0.0131	0.0025	0.0014	0.0013	0.0012
	hand_digits	0.0048	0.0063	0.0031	0.0024	0.0026	0.0017	0.0054	0.0092	0.0018	0.0011	0.0013	0.0006
	image_seg	0.0065	0.0084	0.0095	0.0054	0.0044	0.0044	0.0098	0.0164	0.0113	0.0045	0.0035	0.0036
	isolet	0.0021	0.0023	0.0028	0.0018	\dagger 0.0017	0.0017	0.0078	0.0093	0.0100	0.0044	\dagger 0.0038	0.0038
	letter	0.0077	0.0108	0.0047	0.0042	0.0028	0.0016	0.0857	0.1631	0.0282	0.0245	0.0098	0.0031
	mhr	0.1216	0.1444	0.0951	0.0533	0.0242	0.0324	0.2154	0.2777	0.1269	0.0420	0.0092	0.0147
	molecular	0.0188	0.0388	0.0087	0.0070	0.0069	0.0066	0.0066	0.0294	0.0014	0.0012	0.0011	0.0010
	nursery	0.0179	0.0265	0.0052	\dagger 0.0053	0.0061	0.0058	0.1207	0.2875	0.0138	0.0257	0.0340	0.0259
	obesity	0.0070	0.0072	0.0100	0.0054	0.0084	0.0085	0.0059	0.0065	0.0106	0.0033	0.0095	0.0096
	page_block	0.0141	0.0272	0.0255	0.0169	0.0189	0.0209	0.3351	1.4162	2.1035	0.5741	1.1079	1.4118
	phishing	0.0953	0.1062	0.0503	0.0260	0.0213	0.0234	1.3672	1.4132	0.3629	0.0926	0.0664	0.0802
	satellite	0.0231	0.0312	0.0111	0.0075	0.0070	0.0079	0.0768	0.1463	0.0185	0.0073	0.0058	0.0080
	shuttle	0.0073	0.0093	\dagger 0.0022	0.0057	0.0022	0.0021	0.0028	0.0043	\dagger 0.0004	0.0016	0.0004	0.0003
	waveform-v1	0.0416	0.0582	0.0240	0.0072	0.0100	\dagger 0.0073	0.0234	0.0436	0.0086	0.0007	0.0015	\dagger 0.0008
wine-quality	0.0998	0.1144	0.0618	0.0662	0.1017	0.0714	5.4516	7.6112	\dagger 1.6117	1.5160	6.4950	3.8283	
yeast	0.0539	0.0557	0.0476	0.0623	0.0446	0.0434	7.5742	6.3076	5.5444	10.1276	5.7306	4.9885	
text	gasp	0.0900	0.1199	0.0503	0.0446	\dagger 0.0415	0.0409	0.6272	1.2870	0.1595	0.1084	\dagger 0.1230	\dagger 0.1134
	hcr	0.1265	0.1524	0.0840	0.0848	0.0809	0.0780	0.3778	0.4836	0.1616	\dagger 0.1729	\dagger 0.1781	\dagger 0.1662
	omd	0.1062	0.1181	0.0825	0.0725	0.0609	\dagger 0.0624	0.1845	0.2356	0.1176	0.0952	0.0670	\dagger 0.0749
	sanders	0.1114	0.1341	0.0534	0.0415	0.0454	0.0473	0.5176	0.6638	0.1101	0.0696	0.0841	0.0942
	semeval13	0.1115	0.1364	0.0653	0.0722	\dagger 0.0536	0.0529	0.2692	0.5069	0.0869	0.1059	0.0566	0.0536
	semeval14	0.1039	0.1332	0.0587	0.0659	0.0536	0.0525	0.2100	0.4723	0.0678	0.1075	\dagger 0.0727	\dagger 0.0721
	semeval15	0.1254	0.1425	0.0900	0.0848	0.0823	0.0862	0.2884	0.4532	0.1458	0.1121	0.1374	0.1505
	semeval16	0.1389	0.1611	0.1261	\dagger 0.1101	0.1082	\dagger 0.1087	0.5126	0.6855	0.6068	0.3997	0.4494	0.4573
	sst	0.1050	0.1352	0.0702	0.0562	0.0532	0.0522	0.1685	0.2659	0.0826	0.0509	0.0465	0.0450
	wa	0.0784	0.0819	0.0500	0.0484	0.0432	\dagger 0.0445	0.0874	0.0938	0.0368	0.0339	0.0288	\dagger 0.0306
	wb	0.0804	0.0799	0.0432	\dagger 0.0356	0.0356	\dagger 0.0359	0.1002	0.0990	0.0312	\dagger 0.0204	0.0202	0.0205
	LeQua2022-T1A	0.0933	0.1181	0.0326	\dagger 0.0247	\dagger 0.0243	0.0242	0.1261	0.2024	0.0180	\dagger 0.0101	\dagger 0.0098	0.0097
	LeQua2022-T1B	0.0140	0.0165	0.0122	0.0119	0.0109	0.0109	\dagger 91.1317	118.7730	199.2715	89.9244	99.0783	99.0695
	LeQua2024-T1	0.0862	0.1167	0.0265	0.0218	\dagger 0.0207	0.0204	0.1114	0.1978	0.0125	0.0085	\dagger 0.0079	0.0078
LeQua2024-T2	0.0171	0.0190	0.0145	0.0136	\dagger 0.0138	0.0139	137.5365	163.6220	206.9347	101.0987	152.2147	171.8516	
image	CIFAR100	0.0025	0.0028	0.0028	0.0017	0.0018	0.0017	0.1375	0.1695	0.1797	0.0602	0.0692	0.0659
	CIFAR10	0.0065	0.0080	0.0046	0.0041	0.0043	0.0036	0.0092	0.0127	0.0039	0.0031	0.0034	0.0024
	MNIST	0.0017	0.0018	0.0019	0.0021	0.0020	0.0019	\dagger 0.0007	0.0007	0.0007	0.0007	0.0008	0.0007
	fashionMNIST	0.0083	0.0104	0.0049	0.0046	0.0044	0.0044	0.0201	0.0274	0.0056	0.0049	\dagger 0.0042	0.0042
	SVHN	0.0099	0.0106	0.0061	0.0056	0.0052	0.0047	0.0235	0.0284	0.0088	0.0073	0.0067	0.0055
Rank	4.6	5.6	3.9	2.9	2.1	1.9	4.5	5.5	3.9	2.6	2.5	2.1	

Table 8: Coverage before and after temperature calibration. Left: hard coverage; right: soft coverage. Highlighted cells indicate values within the range $95\% \pm 5\%$.

	Hard Coverage								Soft Coverage												
	Boots-CC		Boots-PCC		Bayes-ACC		Bayes-EMQ (MAPLS)		Bayes-KDEy(Gau)		Bayes-KDEy(Ait- λ)		Bayes-ACC ^{cat}		Bayes-EMQ (MAPLS) ^{cat}		Bayes-KDEy(Gau) ^{cat}		Bayes-KDEy(Ait- λ) ^{cat}		
	Temperature=1				Calibrated Temperature				Temperature=1				Calibrated Temperature								
tabular	abalone	0	0	2	8	0	0	86	51	83	85	21	8	58	66	34	45	95	88	93	94
	academic-success	4	1	73	82	88	89	42	95	88	89	17	8	75	85	87	89	53	96	87	89
	chess	0	0	91	35	60	49	93	57	84	78	23	9	96	79	88	83	97	87	95	93
	cmc	1	0	79	20	24	27	79	49	53	50	10	2	80	44	48	50	80	61	65	63
	connect-4	3	0	96	90	96	97	96	90	96	97	14	6	96	89	96	96	96	89	96	96
	digits	88	79	95	94	95	95	94	94	94	95	97	95	99	98	99	99	98	99	99	99
	dry-bean	54	20	98	95	98	98	96	96	97	97	86	72	100	99	100	100	98	98	98	98
	hand_digits	78	41	95	92	95	95	93	92	93	95	94	86	99	98	99	99	98	98	99	99
	image_seg	61	44	85	82	89	89	45	56	74	74	89	83	91	92	96	96	81	86	91	91
	isolet	88	55	75	71	75	75	73	66	74	72	98	96	99	97	99	99	98	97	98	98
	letter	5	0	74	71	73	75	63	60	62	75	76	48	98	96	98	99	93	92	95	99
	mhr	3	0	67	47	87	69	67	93	100	100	16	6	66	59	88	76	66	96	100	100
	molecular	55	21	99	99	100	100	99	99	100	100	69	39	99	99	100	100	99	99	100	100
	nursery	42	21	99	97	99	99	97	96	96	95	70	56	100	99	100	99	98	97	96	97
	obesity	73	65	96	80	69	67	66	84	69	67	91	89	95	94	88	88	84	96	88	88
	page_block	66	16	69	64	43	35	30	64	64	53	79	46	79	78	72	68	64	78	81	77
	phishing	3	1	82	75	78	75	45	91	92	91	17	10	83	78	84	80	58	90	92	90
	satellite	12	3	97	92	98	90	97	93	98	90	60	46	97	96	98	95	97	97	98	95
	shuttle	92	74	100	98	100	100	100	97	99	100	94	85	100	99	100	100	100	97	100	100
	waveform-v1	16	6	87	98	99	100	54	98	90	96	37	22	86	99	98	100	64	99	91	96
wine-quality	0	0	91	45	28	14	91	85	86	95	15	4	93	70	63	52	93	93	93	96	
yeast	0	0	63	0	0	0	27	34	92	92	23	12	85	30	44	46	70	77	95	95	
text	gasp	37	11	96	90	95	96	96	79	87	87	54	28	97	92	97	96	97	85	90	89
	hcr	19	3	92	58	76	80	97	86	89	91	40	17	94	71	84	86	98	91	93	94
	omd	28	22	92	67	94	92	76	67	84	79	47	38	92	76	96	93	80	76	86	84
	sanders	25	4	96	95	93	91	96	95	93	91	46	22	97	96	95	95	97	96	95	95
	semeval13	28	12	91	76	93	93	91	76	93	93	48	32	94	81	95	96	94	81	95	96
	semeval14	28	13	94	77	94	95	94	77	94	95	50	32	96	84	95	96	96	84	95	96
	semeval15	21	12	73	61	76	74	73	61	76	74	42	30	81	72	82	83	81	72	82	83
	semeval16	18	4	88	64	87	87	93	84	87	87	39	18	89	73	89	89	93	89	89	89
	sst	28	15	92	86	92	93	92	86	92	93	48	35	94	91	94	95	94	91	94	95
	wa	43	34	91	88	90	91	78	73	75	77	61	54	94	90	93	93	84	80	84	83
	wb	43	37	95	94	96	96	95	88	88	89	59	56	97	96	98	98	97	91	91	91
	LeQua2022-T1A	32	21	96	96	98	97	96	89	93	91	32	21	96	96	98	97	96	89	93	91
	LeQua2022-T1B	0	0	42	1	11	13	42	22	42	41	52	30	93	66	84	84	93	87	94	94
	LeQua2024-T1	34	18	98	95	98	98	90	89	91	92	34	18	98	95	98	98	90	89	91	92
LeQua2024-T2	0	0	40	1	17	11	40	17	42	39	41	22	93	69	84	82	93	86	95	94	
image	CIFAR100	0	0	8	4	7	6	4	4	7	6	82	60	96	92	95	94	89	92	95	94
	CIFAR10	90	54	90	88	90	90	88	88	89	90	97	89	99	98	99	99	97	98	98	98
	MNIST	100	90	90	90	90	90	90	90	90	90	100	99	99	98	99	99	99	99	99	99
	fashionMNIST	65	29	90	86	90	90	86	82	88	88	91	82	98	97	99	99	97	96	98	98
	SVHN	71	36	89	89	89	90	83	88	86	89	92	83	98	98	99	99	96	97	97	98
Mean	35	21	82	70	76	74	77	76	83	83	56	43	92	85	89	89	89	90	93	93	

Table 9: Amplitude before and after temperature calibration. Highlighted cells indicate values $\leq 5\%$.

		Boots-CC	Boots-PCC	Bayes-ACC	Bayes-EMQ (MAPLS)	Bayes-KDEy(Gau)	Bayes-KDEy(Ait- λ)	Bayes-ACC ^{cal}	Bayes-EMQ (MAPLS) ^{cal}	Bayes-KDEy(Gau) ^{cal}	Bayes-KDEy(Ait- λ) ^{cal}
		Temperature=1						Calibrated Temperature			
tabular	abalone	< 0.1	< 0.1	< 0.1	< 0.1	< 0.1	< 0.1	44.9	3.3	26.0	30.0
	academic-success	0.4	0.2	2.2	1.0	1.0	1.0	1.1	2.0	1.0	1.0
	chess	< 0.1	< 0.1	0.1	< 0.1	< 0.1	< 0.1	0.4	0.1	< 0.1	< 0.1
	cmc	0.5	0.1	12.5	3.2	3.0	2.9	12.5	6.1	5.9	5.6
	connect-4	0.5	0.1	2.7	1.8	1.6	1.6	2.7	1.8	1.6	1.6
	digits	< 0.1	< 0.1	< 0.1	< 0.1	< 0.1	< 0.1	< 0.1	< 0.1	< 0.1	< 0.1
	dry-bean	< 0.1	< 0.1	< 0.1	< 0.1	< 0.1	< 0.1	< 0.1	< 0.1	< 0.1	< 0.1
	hand_digits	< 0.1	< 0.1	< 0.1	< 0.1	< 0.1	< 0.1	< 0.1	< 0.1	< 0.1	< 0.1
	image_seg	< 0.1	< 0.1	< 0.1	< 0.1	< 0.1	< 0.1	< 0.1	< 0.1	< 0.1	< 0.1
	isolet	< 0.1	< 0.1	< 0.1	< 0.1	< 0.1	< 0.1	< 0.1	< 0.1	< 0.1	< 0.1
	letter	< 0.1	< 0.1	< 0.1	< 0.1	< 0.1	< 0.1	< 0.1	< 0.1	< 0.1	< 0.1
	mhr	0.4	0.1	6.4	1.9	1.1	1.1	6.4	15.3	10.1	9.9
	molecular	0.4	0.4	0.5	0.4	0.4	0.4	0.5	0.4	0.4	0.4
	nursery	< 0.1	< 0.1	0.1	< 0.1	< 0.1	< 0.1	< 0.1	< 0.1	< 0.1	< 0.1
	obesity	< 0.1	< 0.1	< 0.1	< 0.1	< 0.1	< 0.1	< 0.1	< 0.1	< 0.1	< 0.1
	page_block	< 0.1	< 0.1	0.2	< 0.1	< 0.1	< 0.1	0.1	< 0.1	0.1	0.1
	phishing	0.4	0.2	3.4	0.9	0.8	0.8	1.7	1.4	1.1	1.2
	satellite	< 0.1	< 0.1	< 0.1	< 0.1	< 0.1	< 0.1	< 0.1	< 0.1	< 0.1	< 0.1
	shuttle	0.3	0.3	0.3	0.3	0.3	0.3	0.2	0.2	0.2	0.2
	waveform-v1	0.4	0.3	0.9	0.5	0.5	0.5	0.4	0.5	0.2	0.2
wine-quality	< 0.1	< 0.1	5.7	0.8	1.6	0.2	5.7	7.9	15.3	59.0	
yeast	< 0.1	< 0.1	0.3	< 0.1	< 0.1	< 0.1	< 0.1	0.4	28.2	29.9	
text	gasp	4.3	2.2	10.3	6.9	7.8	7.5	10.3	3.6	4.0	3.9
	hcr	4.5	1.2	21.0	8.2	12.7	12.9	36.0	30.7	22.9	23.3
	omd	4.4	3.8	17.4	7.3	12.8	12.4	9.6	7.3	6.8	6.6
	sanders	4.3	1.6	12.0	8.6	8.6	8.4	12.0	8.6	8.6	8.4
	semeval13	4.2	3.1	11.2	7.2	9.0	9.2	11.2	7.2	9.0	9.2
	semeval14	4.3	3.1	11.5	7.2	9.0	9.2	11.5	7.2	9.0	9.2
	semeval15	4.2	3.1	12.0	7.6	9.6	10.0	12.0	7.6	9.6	10.0
	semeval16	4.6	1.4	28.3	12.3	20.9	21.1	36.6	39.5	20.9	21.1
	sst	4.5	4.2	17.3	9.9	10.5	10.5	17.3	9.9	10.5	10.5
	wa	4.2	4.1	8.7	6.5	6.3	6.8	4.5	3.4	3.2	3.5
	wb	4.2	4.1	8.7	6.1	6.3	6.2	8.7	3.2	3.2	3.2
	LeQua2022-T1A	11.3	8.8	18.1	14.5	14.9	14.5	18.1	10.3	10.6	10.3
	LeQua2022-T1B	< 0.1	< 0.1	< 0.1	< 0.1	< 0.1	< 0.1	< 0.1	< 0.1	< 0.1	< 0.1
	LeQua2024-T1	11.1	8.3	16.6	13.0	13.2	13.2	11.8	9.3	9.4	9.4
LeQua2024-T2	< 0.1	< 0.1	< 0.1	< 0.1	< 0.1	< 0.1	< 0.1	< 0.1	< 0.1	< 0.1	
image	CIFAR100	< 0.1	< 0.1	< 0.1	< 0.1	< 0.1	< 0.1	< 0.1	< 0.1	< 0.1	< 0.1
	CIFAR10	< 0.1	< 0.1	< 0.1	< 0.1	< 0.1	< 0.1	< 0.1	< 0.1	< 0.1	< 0.1
	MNIST	< 0.1	< 0.1	< 0.1	< 0.1	< 0.1	< 0.1	< 0.1	< 0.1	< 0.1	< 0.1
	fashionMNIST	< 0.1	< 0.1	< 0.1	< 0.1	< 0.1	< 0.1	< 0.1	< 0.1	< 0.1	< 0.1
	SVHN	< 0.1	< 0.1	< 0.1	< 0.1	< 0.1	< 0.1	< 0.1	< 0.1	< 0.1	< 0.1
Mean	1.7	1.2	5.4	3.0	3.6	3.6	6.6	4.5	5.2	6.4	

Table 10: Pairwise symbolic matrix of Wilcoxon-Holm comparisons on AE.

	Boots-CC	Boots-PCC	Bayes-ACC	Bayes-EMQ (MAPLS)	Bayes-KDEy(Gau)	Bayes-KDEy(Ait- λ)
Boots-CC	=	≪	≫	≫	≫	≫
Boots-PCC	≫	=	≫	≫	≫	≫
Bayes-ACC	≪	≪	=	>	≫	≫
Bayes-EMQ (MAPLS)	≪	≪	<	=	>	>
Bayes-KDEy(Gau)	≪	≪	≪	<	=	≈
Bayes-KDEy(Ait- λ)	≪	≪	≪	<	≈	=

Table 11: Ablation results in terms of AE and W for the unregularized geometry-aware model KDEy(Ait) (i.e., $\lambda = 0$). All methods included for reference. The method is competitive on many datasets, but suffers from instability in a small number of cases; these failure modes are mitigated by the proposed shrinkage regularization. The shrinkage parameter chosen by KDEy(Ait- λ) is shown in the last column.

	AE						W						λ			
	CC	PCC	BBSE/ACC	MLLS/EMQ	KDEy(Gau)	KDEy(Ait)	KDEy(Ait- λ)	CC	PCC	BBSE/ACC	MLLS/EMQ	KDEy(Gau)		KDEy(Ait)	KDEy(Ait- λ)	
tabular	abalone	0.0450	0.0424	0.0966	0.0655	0.0496	0.0485	0.0505	7.0645	6.2734	96.8502	15.7999	9.7935	10.1485	9.8538	0.750
	academic-success	0.0953	0.1211	0.0491	0.0260	0.0251	0.0211	0.0236	0.2541	0.4139	0.0796	0.0231	0.0210	0.0152	0.0188	0.250
	chess	0.0413	0.0450	0.0409	0.0398	\dagger 0.0165	0.0169	0.0163	1.9618	2.3372	1.1529	1.3512	0.3125	\dagger 0.3125	0.3878	0.500
	cmc	0.1560	0.1778	0.1065	0.0973	\dagger 0.0937	0.0965	0.0934	0.3903	0.4937	0.2123	0.1884	\dagger 0.1913	0.2046	\dagger 0.1925	0.999
	connect-4	0.1138	0.1468	0.0270	0.0301	\dagger 0.0205	\dagger 0.0209	0.0201	1.0574	1.6642	0.0742	0.1020	0.0412	\dagger 0.0460	0.0395	0.750
	digits	0.0035	0.0045	0.0030	0.0023	0.0024	0.0016	0.0016	0.0034	0.0045	0.0017	0.0012	0.0014	0.0005	\dagger 0.0006	0.001
	dry-bean	0.0088	0.0122	0.0040	0.0032	0.0032	0.0028	0.0030	0.0066	0.0131	0.0020	0.0012	0.0011	0.0007	0.0010	0.250
	hand_digits	0.0048	0.0063	0.0031	0.0023	0.0023	0.0020	0.0016	0.0054	0.0092	0.0018	0.0010	0.0011	0.0008	0.0006	0.001
	image_seg	0.0063	0.0083	0.0090	0.0051	0.0041	0.0054	0.0041	0.0098	0.0164	0.0114	0.0046	0.0033	0.0046	0.0034	0.900
	isolet	0.0021	0.0023	0.0018	0.0014	0.0014	0.0030	0.0013	0.0077	0.0092	0.0051	0.0034	0.0029	0.0165	0.0027	0.250
	letter	0.0077	0.0108	0.0048	0.0043	0.0025	0.0017	0.0014	0.0856	0.1631	0.0300	0.0253	0.0078	0.0041	0.0025	0.001
	mhr	0.1216	0.1444	0.1113	0.0549	0.0257	0.1445	0.0340	0.2154	0.2776	0.1621	0.0443	0.0104	0.3019	0.0164	0.250
	molecular	0.0188	0.0388	0.0089	0.0071	0.0072	0.0064	0.0068	0.0066	0.0294	0.0014	0.0013	0.0011	0.0010	0.0011	0.500
	nursery	0.0179	0.0265	0.0050	\dagger 0.0051	0.0061	0.0096	0.0069	0.1206	0.2875	0.0139	0.0256	0.0703	0.1424	0.0474	0.001
	obesity	0.0070	0.0072	0.0095	0.0050	0.0084	0.0074	0.0085	0.0059	0.0065	0.0102	0.0029	0.0092	0.0059	0.0093	0.900
	page_block	0.0141	0.0271	0.0217	0.0170	0.0194	0.0163	0.0215	0.3355	1.4168	1.4289	0.5930	1.1913	0.5861	1.5181	0.999
	phishing	0.0953	0.1062	0.0553	0.0281	0.0221	0.0549	0.0243	1.3672	1.4128	0.4169	0.1092	0.0717	0.5383	0.0872	0.999
	satellite	0.0231	0.0312	0.0111	0.0076	0.0070	0.0066	0.0078	0.0767	0.1463	0.0194	0.0077	\dagger 0.0059	0.0055	0.0078	0.250
	shuttle	0.0073	0.0093	0.0021	0.0054	0.0019	0.0020	0.0018	0.0028	0.0043	0.0004	0.0014	0.0003	0.0004	0.0002	0.900
	waveform-v1	0.0416	0.0582	0.0250	\dagger 0.0070	0.0102	0.0069	0.0073	0.0234	0.0436	0.0094	0.0007	0.0015	\dagger 0.0007	0.0008	0.001
wine-quality	0.0998	0.1144	0.0879	0.0714	0.1328	0.1511	\dagger 0.0729	5.4520	7.6107	2.9600	1.6965	9.9969	13.4015	3.8726	0.250	
yeast	0.0539	0.0557	0.0561	0.0647	0.0449	0.0409	0.0437	7.5748	6.3074	6.7092	11.1195	5.8082	3.5281	5.0089	0.999	
text	gasp	0.0899	0.1199	0.0518	0.0415	0.0409	0.0393	\dagger 0.0397	0.6271	1.2881	0.1704	\dagger 0.1001	0.1149	0.0973	\dagger 0.1011	0.250
	hcr	0.1265	0.1524	0.0962	0.0811	0.0814	0.0731	0.0793	0.3777	0.4836	0.2078	0.1610	0.1737	0.1382	0.1635	0.500
	omd	0.1062	0.1182	0.0901	0.0688	\dagger 0.0620	\dagger 0.0630	0.0618	0.1844	0.2356	0.1412	0.0876	0.0715	\dagger 0.0720	\dagger 0.0745	0.500
	sanders	0.1114	0.1341	0.0587	\dagger 0.0470	0.0459	\dagger 0.0464	\dagger 0.0463	0.5178	0.6633	0.1318	0.0930	0.0839	\dagger 0.0855	0.0892	0.900
	semeval13	0.1115	0.1365	0.0758	0.0739	0.0580	0.0597	\dagger 0.0589	0.2692	0.5073	0.1111	0.1040	0.0642	0.0676	\dagger 0.0658	0.001
	semeval14	0.1038	0.1332	0.0668	0.0656	0.0560	0.0576	\dagger 0.0568	0.2100	0.4723	0.0967	0.1070	0.0776	0.0834	0.0818	0.001
	semeval15	0.1253	0.1425	0.0958	\dagger 0.0865	0.0863	0.0915	0.0913	0.2880	0.4533	0.1585	0.1124	0.1520	0.1734	0.1715	0.001
	semeval16	0.1389	0.1612	0.1891	0.1110	0.1370	0.1354	0.1390	0.5124	0.6856	1.1685	0.4215	0.6520	0.6326	0.6749	0.500
	sst	0.1051	0.1352	0.0749	\dagger 0.0539	0.0541	0.0575	0.0538	0.1687	0.2659	0.0904	\dagger 0.0487	0.0490	0.0560	0.0484	0.999
	wa	0.0783	0.0819	0.0517	0.0500	\dagger 0.0425	0.0412	0.0432	0.0873	0.0938	0.0393	0.0370	\dagger 0.0281	0.0264	0.0297	0.001
	wb	0.0804	0.0799	0.0439	0.0333	0.0343	0.0348	0.0346	0.1001	0.0990	0.0316	0.0183	0.0190	0.0197	0.0194	0.250
LeQua2022-T1A	0.0933	0.1181	0.0314	\dagger 0.0240	0.0242	\dagger 0.0252	0.0234	0.1260	0.2024	0.0170	\dagger 0.0099	\dagger 0.0097	\dagger 0.0114	0.0093	0.001	
LeQua2022-T1B	0.0140	0.0165	0.0130	\dagger 0.0119	0.0118	0.0171	0.0118	91.1316	118.7259	121.7791	92.8496	109.3588	141.3354	109.3062	0.999	
LeQua2024-T1	0.0862	0.1167	0.0270	\dagger 0.0205	0.0204	0.0232	\dagger 0.0206	0.1114	0.1978	0.0130	\dagger 0.0078	0.0078	0.0103	\dagger 0.0079	0.250	
LeQua2024-T2	0.0171	0.0190	0.0170	0.0137	0.0160	0.0256	0.0156	137.5911	163.6366	231.3429	100.8582	186.1994	318.9042	196.3228	0.900	
image	CIFAR100	0.0025	0.0028	0.0022	0.0016	0.0018	0.0021	0.0017	0.1375	0.1695	0.1009	0.0576	0.0712	0.1118	0.0643	0.250
	CIFAR10	0.0065	0.0080	0.0044	0.0036	0.0038	0.0035	0.0036	0.0092	0.0127	0.0037	0.0025	0.0027	0.0023	0.0024	0.001
	MNIST	0.0016	0.0018	0.0017	0.0012	0.0012	0.0020	0.0011	0.0007	0.0006	0.0005	0.0003	0.0003	0.0008	0.0003	0.001
	fashionMNIST	0.0083	0.0103	0.0047	0.0041	0.0038	\dagger 0.0039	0.0038	0.0201	0.0274	0.0052	0.0041	0.0036	\dagger 0.0036	0.0036	0.999
	SVHN	0.0098	0.0106	0.0061	0.0053	0.0049	0.0046	0.0045	0.0235	0.0284	0.0091	0.0072	0.0060	0.0051	\dagger 0.0052	0.001
Rank	5.4	6.5	5.0	3.1	2.6	3.2	2.2	5.3	6.3	4.8	3.0	2.7	3.3	2.6	—	